Title: The South Atlantic Circulation between 34.5ºS, 24ºS and above the Mid-Atlantic Ridge from an Inverse Box Model

Authors: Cristina Arumí-Planas[1], María Dolores Pérez-Hernández[1], Josep L. Pelegrí[2], Pedro Vélez-Belchí[3], Mikhail Emelianov[2], Verónica Caínzos[1], Luis Cana[1], Yvonne L. Firing[4], Luis García-Weil[5], Daniel Santana-Toscano[1], Alonso Hernández-Guerra[1]

[1]Unidad Océano y Clima, Instituto de Oceanografía y Cambio Global, IOCAG, Universidad de Las Palmas de Gran Canaria, ULPGC, Unidad Asociada ULPGC-CSIC, Las Palmas de Gran Canaria, Spain,
[2]Departament d'Oceanografia Física i Tecnològica, Institut de Ciències del Mar, CSIC, Unidad Asociada ULPGC-CSIC, Barcelona, Spain,
[3]Centro Oceanográfico de Canarias, Instituto Español de Oceanografía, CSIC, Santa Cruz de Tenerife, Spain,
[4]National Oceanography Centre, European Way, Southampton, United Kingdom SO31 5Bz,
[5]Instituto Universitario de Estudios Ambientales y Recursos Naturales (i-UNAT), Universidad de Las Palmas de Gran Canaria, ULPGC, Las Palmas de Gran Canaria, Spain.

Key points

- The upper layers present the course of the anticyclonic South Atlantic subtropical gyre and the northeast route of the Benguela Current.
- The deep layers present the southward flowing boundary currents and an eastward interbasin flow close to 24ºS above the Mid-Atlantic Ridge.
- The heat transport flows northward across the subtropical South Atlantic Ocean, where evaporation dominates over precipitation.

Abstract

The South Atlantic Ocean plays a key role in the heat exchange of the climate system, as it hosts the returning flow of the Atlantic Meridional Overturning Circulation (AMOC). To gain insights on this role, using data from three hydrographic cruises conducted in the South Atlantic Subtropical gyre at 34.5ºS, 24ºS and 10ºW, we identify water masses and compute absolute geostrophic circulation using inverse modeling. In the upper layers, the currents describe the South Atlantic anticyclonic gyre with the northwest flowing Benguela Current (-16.3±2.0 Sv at 34.5ºS, and 21.2±1.8 Sv at 24ºS) flowing above the Mid-Atlantic Ridge (MAR) between 22.4ºS-28.4ºS (-19.2±1.4 Sv), and the southward flowing Brazil Current (-16.5±1.3 Sv at 34.5ºS, and -7.3±0.9 Sv at 24ºS); the deep layers feature the southward transports of Deep Western Boundary Current (DWBC; -13.9±3.0 Sv at 34.5ºS, and -8.7±3.8 Sv at 24ºS) and Deep Eastern Boundary Current (DEBC; -15.1±3.5 Sv at 34.5ºS, and -16.3±4.7 Sv at 24ºS), with the interbasin west-to-east flow close to 24ºS (7.5±4.4 Sv); the abyssal waters present northward mass transports through the Argentina Basin (5.6±1.1 Sv at 34.5ºS, and 5.8±1.5 Sv at 24ºS) and Cape Basin (8.6±3.5 Sv at 34.5ºS to 3.0±0.8 Sv at 24ºS) before returning southward (-2.2±0.7 Sv at 24ºS to -7.9±3.6 Sv at 34.5ºS), without any interbasin exchange across the MAR. In addition, we compute the upper AMOC strength (14.8±1.0 and 17.5±0.9 Sv), the equatorward heat transport (0.30±0.05 and 0.80±0.05 PW), and the freshwater flux (0.18±0.02 and -0.07±0.02 Sv) at 34.5ºS and 24ºS, respectively.

Plain language summary

The location of the South Atlantic subtropical gyre plays a critical role in the Atlantic Meridional Overturning Circulation, which controls the Earth's climate system. We have examined the South Atlantic subtropical gyre's circulation between 34.5ºS and 24ºS and above the Mid-Atlantic Ridge using data from three hydrographic cruises (34.5ºS, 24ºS and 10ºW). From these cruises, we have identified the water masses present on this region and computed their transport. Thus, we describe the path of the anticyclonic gyre and the northeast route of the Benguela Current in the upper water masses (<1440 m depth); the southward flowing western and eastern boundary currents and an eastward interbasin flow close to 24ºS above the Mid-Atlantic Ridge in the deep water masses (those on the depth range from 1440 to 3800 m depth); and the northward flow of the abyssal water masses (>3800 m depth). We have also reported the characteristic heat transport flowing northward across the subtropical South Atlantic Ocean, where evaporation dominates over precipitation.

This article has been accepted for publication and undergone full peer review but has not been through the copyediting, typesetting, pagination and proofreading process, which may lead to differences between this version and the Version of Record. Please cite this article as doi: 10.1029/2022JC019614.

Keywords
Physical Oceanography, Climate Change, Ocean Circulation, South Atlantic Ocean, Mid-Atlantic Ridge, Inverse Model.

1. Introduction

The Earth's climate system is regulated by both ocean and atmosphere, which on average transfer heat from the equator to the subpolar regions. The South Atlantic Ocean plays an important and distinctive role in this heat exchange, as it hosts the returning flow of the Atlantic Meridional Overturning Circulation (AMOC), with its warm upper-ocean currents transporting heat northward from the subtropics to the tropics, hence compensating the southward flow of the cold and dense North Atlantic Deep Water (NADW) (Ganachaud & Wunsch, 2000; Garzoli et al., 2013; Talley, 2003). The Atlantic Ocean is different from all ocean basins because of the resulting net northward heat transport at all latitudes (Kelly et al., 2014), and it plays a major role in modulating European (e.g., Moffa-Sánchez & Hall, 2017; Palter, 2015) and global (e.g., Buckley & Marshall, 2016; Lynch-Stieglitz, 2017) climates.

The AMOC's upper limb is predominantly supplied by waters entering the South Atlantic via the Drake Passage and the Malvinas Current, the so-called "cold water route", or via the Agulhas Current and the Agulhas leakage, the "warm water route" (Gordon, 1986; Speich et al., 2001). Off the west coast of southern Africa is found the Benguela Current is found in the upper and intermediate layers, which forms the eastern boundary current of the anticyclonic South Atlantic subtropical gyre. The Benguela Current is supplied by both the South Atlantic Current, flowing along the southern margin of the South Atlantic subtropical gyre (≈ 5 Sv), and by South Indian Ocean waters via the Agulhas Current (≈ 10 Sv) in the upper ~1500 m of the South Atlantic Ocean (Gordon et al., 1992; Guo et al., 2023; Peterson & Stramma, 1991).

The Deep Western Boundary Current (DWBC) carries deep water from the Labrador Sea and the North Atlantic's Overflow Water layers to the southern latitudes (Talley & McCartney, 1982). The DWBC is the primary southward pathway for the cold and lower limb of the AMOC and has been extensively studied in the North Atlantic Ocean (e.g. Meinen & Garzoli, 2014; Toole et al., 2011). The deep pathways of the AMOC in the South Atlantic Ocean, however, are not as well documented (Garzoli et al., 2015). Arhan et al. (2003) confirmed two eastward pathways of NADW near the equator. Arhan et al. (2003) and Reid (1989) suggested similar circulation patterns in the South Atlantic at 2500 m depth, indicating that most of the NADW enters the eastern basin between 20ºS and 25ºS, and then turns southeastward and flows above the Walvis Ridge through passages south of 28ºS, entering the Cape Basin.

The zonal transports at the Mid-Atlantic Ridge (MAR) are crucial for connecting the eastern and western South Atlantic basins. There is one single realization of a meridional hydrographic section in the South Atlantic Ocean close to the MAR, which was done along 9ºW (A14), from 4.3ºN to 45.5ºS during January and February 1995, as part of the World Ocean Circulation Experiment (WOCE) (Arhan et al., 2003; Mercier et al., 2003). To monitor flows across the MAR, the South Atlantic GAteway (SAGA) Array was deployed at the MAR at 10ºW, between 34ºS and 19ºS at about 4000 m depth. The array configuration consists of four pressure-equipped inverted echo sounders (PIES) separated by about 5º of latitude, with deep instrumented moorings located in between.

Our main goal in this study is to use these hydrographic measurements along 10ºW along with an inverse model in order to describe the circulation above the MAR between 34.5ºS and 24ºS in the South Atlantic (Fig. 1). To achieve this objective, we must determine the mass transport of the Brazil Current flowing southward and the northwestward flow of the Benguela Current, in both the thermocline and intermediate layers; the deep ocean currents that carry cold waters from the North Atlantic toward the southern latitudes in the western and eastern basins; as well as the northward flow of the abyssal layers. A significant result of the present study is that we will be able to determine the upper AMOC strength, including the heat and freshwater transports, at both latitudes.

The structure of this paper is outlined as follows. The hydrographic and Ocean General Circulation Model (OGCM) data are described in Section 2. Section 3 presents the vertical sections of different ocean properties to describe the water masses along 34.5ºS, 24ºS and 10ºW in the South Atlantic Ocean. The initial geostrophic transports and the inverse model characteristics are presented in Section 4. This is followed by the final adjusted transports and the resulting AMOC estimate in Section 5. The resulting horizontal circulation for the upper, deep and bottom layers are described in Section 6, the heat and freshwater transports obtained for both latitudes are provided in Section 7, and a scheme of the upper, deep and bottom pathways is shown in Section 8. Finally, Section 9 provides a discussion and concluding remarks on this work.

2. Hydrographic and Ocean General Circulation Model (OGCM) data

For our study we use three hydrographic cruises carried out in the South Atlantic Ocean: 34.5ºS in 2017, 24ºS in 2018, and 10ºW in 2021 (Fig. 1). The hydrographic data at 34.5ºS were collected during the expedition of the German Research Vessel *Maria S. Merian* conducted in summer 2017 (MSM60); the hydrographic data at 24ºS were collected in fall 2018 on the *RRS James Cook* (JC159) as part of the Ocean Regulation of Climate by Heat and Carbon Sequestration and Transports (ORCHESTRA) project and the international Global Ocean Ship-Based Hydrographic Investigations Program (GO-SHIP) (Talley et al., 2016); and the hydrographic data at 10ºW were collected in fall 2021 as part of the SAGA project onboard the R/V *Sarmiento de Gamboa*. The distance between stations was generally ≈50 km, with narrower spacing over boundary currents and steep topographic slopes. At each station, we use vertical profiles of potential temperature and salinity every two decibars as obtained from the conductivity-temperature-depth (CTD) probes. For the three hydrographic cruises, a shipboard acoustic Doppler current profiler (SADCP, of 38 kHz for MSM60 and the SAGA cruise, and 75 kHz for JC159) was employed at each station pair to provide a velocity profile from the sea surface down to depths between 800 and 1500 m. Also, for the 34.5ºS and 10ºW cruises, a velocity profile from the sea surface to the seafloor at each station was obtained from a paired (at 34.5ºS, 300 kHz upward-looking and 150 kHz downward-looking) or single (at 10ºW, 150 kHz downward-looking) lowered acoustic Doppler current profiler (LADCP). As in Hernández-Guerra & Talley (2016) and Hernández-Guerra et al. (2019), the ADCP data will prove to be useful in the inverse model to constrain the boundary currents.

Our hydrographic data are complemented by simulations from two different numerical ocean models. ECCOv4r4 (Estimating the Circulation and Climate of the Ocean Version 4 Release 4; ECCO, hereafter) is a data-assimilating model developed by the Jet Propulsion Laboratory. It incorporates oceanographic observations, such as altimetry-derived sea surface height, hydrography from Argo profilers, ocean bottom pressure from the Gravity Recovery and Climate Experiment (GRACE) and hydrographic and current data from moorings, among others (Fukumori et al., 2020). The adjoint method is applied to repeatedly minimize the squared sum of weighted model-data misfits and control adjustments, improving the fit of the numerical data to the observations (Wang et al., 2020). ECCO provides the state of the ocean's evolution over time on a monthly data basis, with 50 standard levels and a nominal 1/2º (≈ 48 km in our region) horizontal resolution configuration of the Massachusetts Institute of Technology general circulation model over the entire world, covering 26 years from 1992 to 2017 (ECCO Consortium et al., 2020, 2021; Forget et al., 2015).

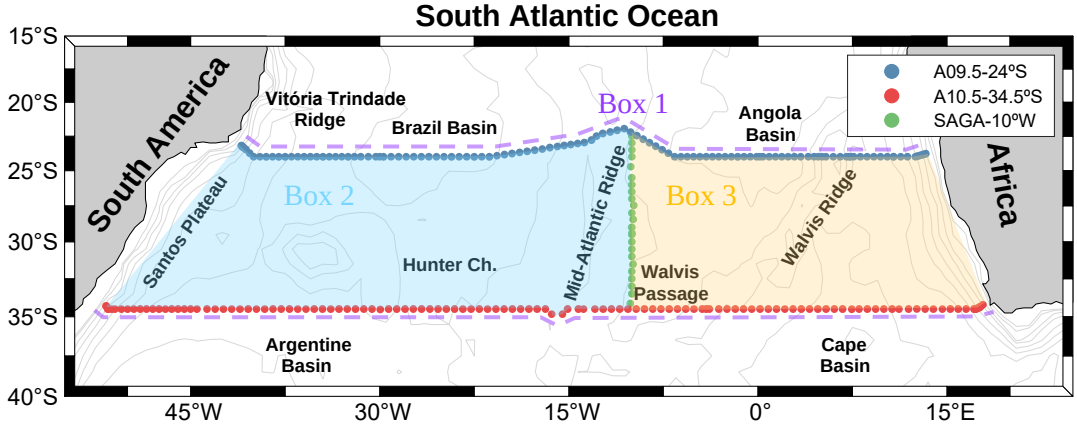

Fig. 1. Positions of the hydrographic stations for the three South Atlantic cruises carried out at nominally 24ºS, 34.5ºS and 10ºW. The different boxes used in this study are identified as Box 1 (purple dashed lines), Box 2 (light blue), and Box 3 (light orange).

The GLORYS12V1 (Global Ocean Physics Reanalysis; GLORYS, hereafter), an ocean model developed by Mercator and distributed by the European Copernicus Marine Environment Monitoring Service (CMEMS), is an eddy-resolving global ocean reanalysis that describes ocean circulation and includes sea-level forcing from satellite altimetry measurements covering the period of 1993 to 2019. GLORYS is developed using the current real-time global forecasting CMEMS system and the Nucleus for European Modelling of the Ocean (NEMO) model-based hydrodynamics. The CORA4 database and the ERA-Interim data are used for assimilating in situ observations and atmospheric forcing, respectively. Additionally, in situ temperature and salinity vertical profiles, altimeter data (sea level anomaly), sea ice concentration and satellite sea surface temperature are assimilated together. This numerical model provides monthly gridded datasets at 1/12º (≈ 8 km in our region) horizontal resolution and 50 vertical levels (Drévillon et al., 2018).

To summarize, the ocean models used (ECCO and GLORYS) are data-assimilating models varying from coarse to eddy-permitting horizontal resolution (1/2º and 1/12º, respectively). After applying the inverse model, mass transports from hydrographic data are compared with monthly data for the whole water column in the South Atlantic Ocean, along 24ºS and 34.5ºS for 2017-2019 (GLORYS) and 2017 (ECCO). No data from these models are yet available for 2021, the year of the 10ºW expedition.

3. Vertical sections and water masses

The existing water masses are identified using the zonal (34.5ºS and 24ºS) and meridional (10ºW) vertical sections of potential temperature, salinity, and oxygen for the three hydrographic cruises following Katsumata & Fukasawa (2011) and Talley et al. (2011) (Fig. 2). The meridional section at 10ºW, just east of and roughly parallel to the MAR, divides the transatlantic sections into western and eastern basins. We have used 11

In the upper layers, the South Atlantic Central Water (SACW) is found between the sea surface and the neutral density γ^n = 27.23 kg/m^3 (above ≈ 730 m depth), with relatively high potential temperature (> 5ºC; Figs. 2a, b, and c), relatively high salinity (> 34.7; Fig. 2d, e, and f), and high dissolved oxygen of about 210-235 µmol/kg (Figs. 2g, and h). This water mass is formed by the subduction of fluid via Ekman pumping out of the mixed layer in the Subtropical Convergence region (Gordon, 1981, 1989; Sprintall & Tomczak, 1993). The SACW is conveyed to the eastern basin by the South Atlantic Current and northwestward through the Benguela Current (Stramma & England, 1999), with a high contribution from the Indian Ocean through the Agulhas Current (warm water route) (Gordon, 1985; Poole & Tomczak, 1999; Sprintall & Tomczak, 1993), including the large and slow contribution of Agulhas rings transporting warm and salty waters into the Atlantic (Casanova-Masjoan et al., 2017).

The upper thermocline layers (γ^n < 27.23 kg/m^3) of the transoceanic vertical sections present titled isotherms and isopycnals that allow us to identify the signals of the Brazil and Benguela Currents in the western and eastern margins, respectively (Fig. 2a, b, d, and e). The thermohaline isolines in the ocean interior indicate equatorward mass transport, as they descend to the west. Below this upper layer, we find the Antarctic Intermediate Water (AAIW) (27.23 kg/m^3 < γ^n < 27.58 kg/m^3, which corresponds to depths between 730 and 1140 m). This water mass presents relatively cold waters of potential temperatures of 3 to 5ºC (Fig. 2a, b, and c), profile-minimum salinity values (34.3 to 34.5; Fig. 2d, e, and f). Its dissolved oxygen concentration is relatively low at 24ºS (< 200 µmol/kg; Fig. 2g) and higher at 34.5ºS (> 220 µmol/kg at 34.5ºS; Fig. 2h). The AAIW is formed in the Southern Ocean, near the Subantarctic Front of the Antarctic Circumpolar Current (ACC) (Talley, 1996). Its formation is driven by a combination of cooling and mixing processes, as well as interactions between ocean currents, such as the ACC, before spreading into the South Atlantic (Matano et al., 2010; Sloyan & Rintoul, 2001). The main AAIW sources to the Atlantic Ocean are from the Southeastern Pacific, entering through the northern Drake Passage, the narrowest gap connecting the South Atlantic and Pacific Oceans between the Antarctic Peninsula and South America, and the Malvinas Current loop, a large clockwise circulation feature in the South Atlantic that flows around the Falkland Islands (Suga & Talley, 1995). At 34.5ºS in the eastern basin of the South Atlantic Ocean, the high salinity of the AAIW density class is attributed to the mixing of older AAIW with the Red Sea Water coming from the Indian Ocean, which has a much higher salinity than that of the AAIW layers located in the southwestern Atlantic Ocean (Shannon & Hunter, 1988). The lower oxygen levels (<180 µmol/kg) in the eastern basin also point to an Indian Ocean

source. This is supported by the fact that the Indian deep waters, which originate from upwelled bottom waters of greater age than those from the Atlantic Ocean sourced from surface waters (Gordon et al., 1992; Talley, 1996, 2013). Specifically, the Indian Ocean presents oxygen levels of 160-220 μmol/kg between 600 and 1200 m depth (McDonagh et al., 2008). The low oxygen concentrations are more noticeable in the 24ºS section, further suggesting that these waters originate from the Indian Ocean and spread westward as they flow north in the Atlantic, before feeding the NADW overturn (Talley, 2013). Also, the minimum salinity patches (< 34.3) in the western basin at 34.5ºS suggest that the northward flow in the ocean interior transports more recently ventilated AAIW (Hernández-Guerra et al., 2019).

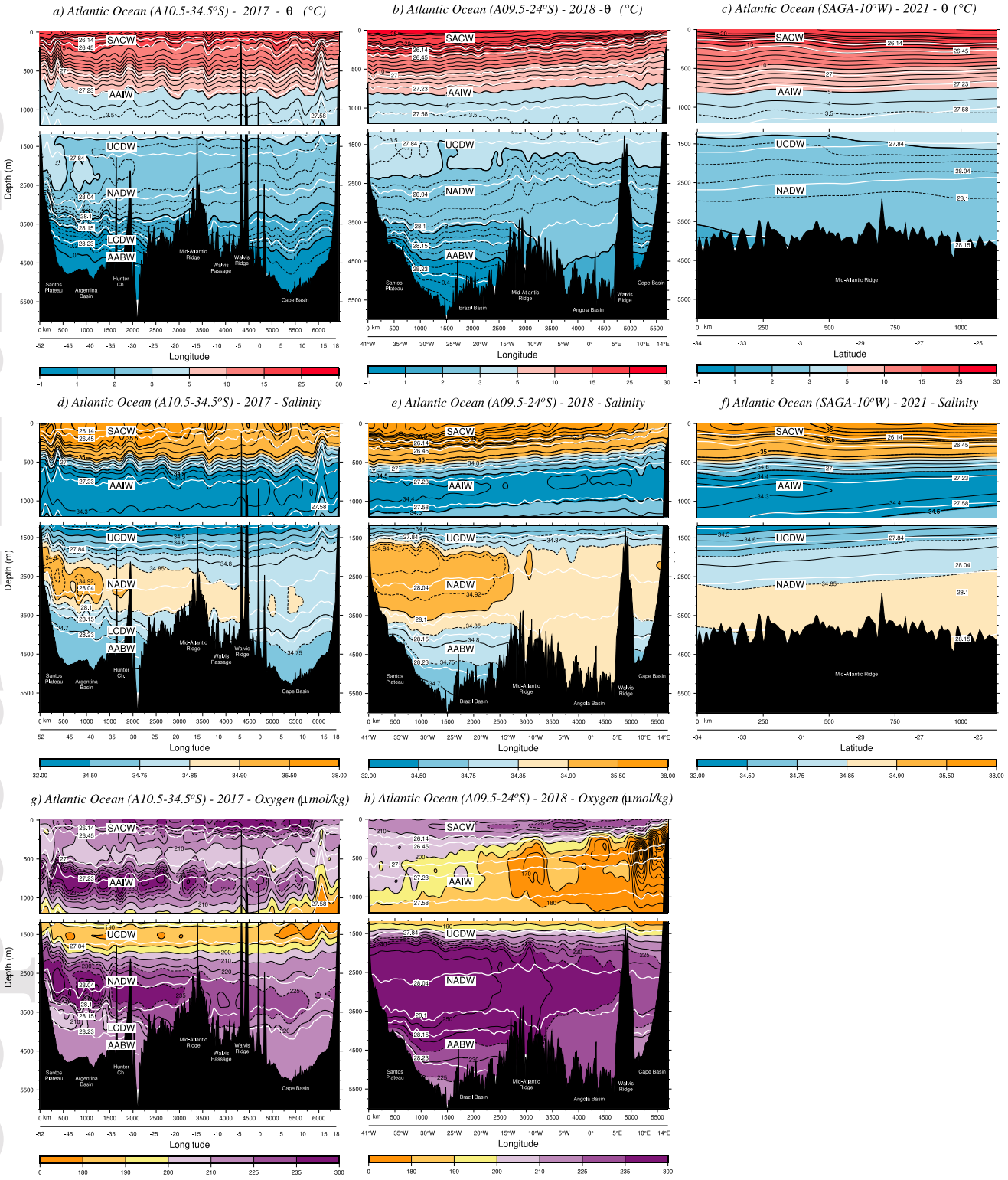

Fig. 2. Vertical sections of (a, b, c) θ (ºC), (d, e, f) salinity, and (g, h) oxygen (µmol/kg) in the South Atlantic Ocean for data collected at 34.5ºS in 2017, at 24ºS in 2018 and at 10ºW in 2021, respectively. The water masses identified are: South Atlantic Central Water (SACW), Antarctic Intermediate Water (AAIW), Upper Circumpolar Deep Water (UCDW), North Atlantic Deep Water (NADW), Lower Circumpolar Deep Water (LCDW), and Antarctic Bottom Water (AABW). The location of stations is indicated with the tick-marks on the top axis indicate the location of stations. The γ^n layers identified by isoneutrals labels (white lines) are those used to compute the geostrophic transport.

In the deep layer, with a neutral density range of 27.58 kg/m^3 < γ^n < 27.84 kg/m^3, extending from about 1140 to 1600 m, we find the core of the Upper Circumpolar Deep Water (UCDW). The UCDW originates from the mixture of deep waters from the Indian, Pacific and Southern Oceans. This is a relatively oxygen-poor (180 to

200 μmol/kg; Fig. 2g, and h), fresh (34.5 to 34.7; Fig. 2d, e, and f), and cold water mass (2.5 to 3ºC; Fig. 2a, b, and c).

NADW is also found in the deep layers, below the UCDW, at depths ranging from about 1600 to 3800 m (27.84 kg/m^3 < γ^n < 28.15 kg/m^3). This water mass is formed as a result of the mixing and aging of deep waters flowing latitudinally toward the Southern Ocean. NADW is identified in the vertical by relatively low potential temperature (1.5 to 2.5ºC; Fig. 2a, b, and c), high salinity (34.85 to 34.9; Fig. 2d, e, and f), and high dissolved oxygen concentration (200 to 250 μmol/kg; Fig. 2g, and h). The properties of the NADW are best observed in the western region, due to the eastward decrease in salinity and oxygen, towards the MAR. Additionally, the presence of the Deep Western Boundary Current (DWBC) shows up as anomalous values of potential temperature (1.53ºC), salinity (34.7) and oxygen (206.7 μmol/kg) near the seafloor (≈ 2800 m depth) at about 50ºW, which contrasts with the respective values of 3.2ºC, 34.9 and 228.9 μmol/kg observed at 2110 m depth (e.g., Reid et al., 1977; Zemba, 1991) (Fig. 2).

The AABW is the densest water mass in the Atlantic, from ≈ 3800 m to the seafloor (γ^n > 28.15 kg/m^3). The AABW is colder (θ < 1.5ºC; Fig. 2a, and b), fresher (34.7 to 34.75; Fig. 2d and e) and has lower dissolved oxygen concentrations (220 to 240 μmol/kg; Fig. 2g and h) than the NADW. The main source of the AABW is the mixed Antarctic waters and the NADW (de Carvalho Ferreira & Kerr, 2017; Heywood & King, 2002; Mantyla & Reid, 1983; Peterson & Whitworth, 1989; Reid et al., 1977). The Walvis Ridge limits the northward flow of AABW in the eastern basin. The hydrographic section at 10ºW is on the MAR with shallower depths than the AABW and, therefore, is not present in this section (Fig. 2c, f, and i). The AABW can be separated into two different components at 34.5ºS. The upper part of the AABW is formed in the Antarctic Circumpolar Current, which is a combination of AABW and NADW, resulting in a new water mass called Lower Circumpolar Deep Water (LCDW) (Mantyla & Reid, 1983; Stramma & England, 1999). The LCDW is the primary water mass in contact with the AABW within the Argentine Basin (Coles et al., 1996), between 28.15 kg/m^3 < γ^n < 28.23 kg/m^3, between about 3800 and 4700 m. These water masses differ only slightly in most of the properties so that they are not clearly separated in the water column (Vanicek & Siedler, 2002). However, at 34.5ºS the LCDW has slightly higher temperatures (≈ 1.0-1.5ºC; Fig. 2a), higher salinity (34.75-34.8; Fig. 2d) and lower dissolved oxygen concentrations (210-220 μmol/kg; Fig. 2g) than the AABW (θ <1ºC, S ≈ 34.7, O_2 ≈ 220 μmol/kg; Fig. 2a, d, and g).

4. Relative geostrophic transport and inverse model

At each station pair, the relative geostrophic velocity is computed using the thermal wind equation so the absolute velocity depends on the chosen reference layer. For section 34.5ºS we choose the NADW-LCDW interface at $\gamma^n = 28.15$ kg/m^3 (≈ 3800 m depth) as reference layer (Fig. 2). Similarly, for sections 24ºS and 10ºW we select the interface UCDW-NADW, located at the neutral density $\gamma^n = 27.84$ kg/m^3 (≈ 1600 m depth) (Fig. 2). If the reference layer is deeper than the deepest common depth of a pair of stations, the bottom is selected as the reference level of no motion.

Otherwise, the SADCP and LADCP data from the sections at 34.5ºS and 10ºW are used to estimate the velocities at the reference level, and only SADCP data from the section at 24ºS (Comas-Rodríguez et al., 2010; Joyce et al., 2001). Figure 3 presents the initial geostrophic velocity (dashed black lines), the average SADCP velocity along the station-station track segment (red line), the mean LADCP velocity from each hydrographic station pair LADCP velocities (blue line), and the geostrophic velocity adjusted to the ADCP velocity (black solid line). The velocity adjustments are performed under four different cases (a through d) for the sections at 34.5ºS, 10ºW and 24ºS. Firstly, if either both SADCP and LADCP (case a) or just SADCP (case b) match the geostrophic velocity profile, then SADCP data is used to adjust the initial geostrophic velocity. Next, if only the LADCP matches the profile of the geostrophic velocity but SADCP does not, then LADCP data is used to adjust the initial geostrophic velocity (case c). When neither the SADCP nor LADCP patterns match the geostrophic velocity profile, then the initial geostrophic velocity is not adjusted (case d). Notice that the LADCP velocities are located at each station rather than over the whole interval over which the geostrophic velocity is computed, while the underway SADCP continuously collects data, so SADCP can better match the location of the geostrophic calculation. Consequently, SADCP data is considered to be more appropriate for estimating the

reference level velocities in most cases (Arumí-Planas et al., 2022). Then, the adjusted reference velocity is estimated as the average velocity of the selected depths in the range of the dashed horizontal lines.

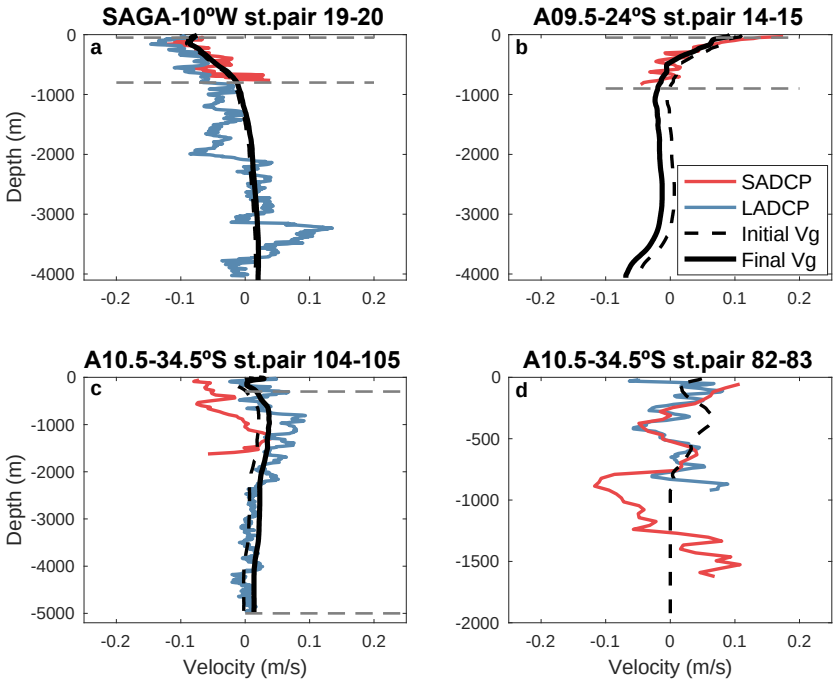

Fig. 3. Comparison between the profiles of the initial geostrophic velocity (dashed black lines), the SADCP (red line) and LADCP (blue line) velocity normal to the station pairs, and the geostrophic velocity adjusted using the SADCP or LADCP data (black solid line) for four different cases of adjustment: (a) geostrophic velocities agree with both SADCP and LADCP data, (b) only SADCP data agree, (c) only LADCP data agree, and (d) neither SADCP nor LADCP data agree.

Mass transports are computed for 11 isoneutral layers following Arumí-Planas et al. (2022), Hernández-Guerra & Talley (2016), Hernández-Guerra et al. (2019), and Talley (2008) (Fig. 2 and 4). The NCEP wind stress is used to calculate the Ekman transports (Kalnay et al., 1996) at the time of each hydrographic cruise (Arumí-Planas et al., 2022; Hernández-Guerra et al., 2019; Hernández-Guerra & Talley, 2016). The resulting Ekman transports, of -1.6±0.1 Sv at 24ºS, 0.1±0.2 Sv at 34.5ºS, and 0.1±0.1 Sv at 10ºW, are included in the uppermost layer of each section.

In our study, there are three enclosed regions (Fig. 1): Box 1 is formed by the combined transatlantic sections at 34.5ºS and 24ºS, and Boxes 2 and 3 are respectively formed by the eastern and western stations of sections 34.5ºS and 24ºS combined with section 10ºW. Figure 4 presents the initial integrated mass transports per layer for each enclosed region in the Atlantic Ocean; these initial estimates use the velocity at the reference layer as obtained from the ADCP data. There is an initial imbalance, integrated over all layers, of 5.3 Sv in Box 1, 30.4 Sv in Box 2, and -25.0 Sv in Box 3 (Table 1; positive and negative values represent divergence and convergence, respectively). The initial fields for the upper and bottom layers have a northward mass transport, while the deep layers present a southward mass transport across both the 34.5ºS and 24ºS transoceanic sections, and a westward and eastward mass transport for upper and deep layers through the 10ºW meridional section, respectively.

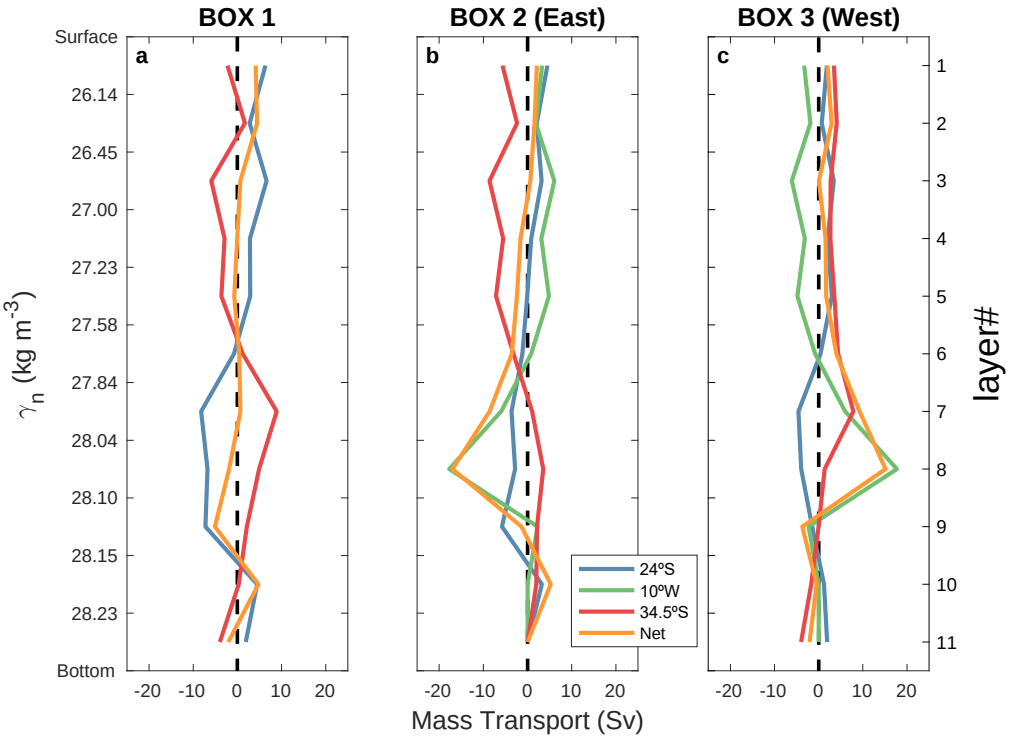

Fig. 4. Initial integrated mass transports (Sv) per neutral density layer at 24ºS (blue line), 10ºW (green line) and 34.5ºS (red line), and the net (orange line) in the South Atlantic Ocean. The three panels correspond to the mass transport in (a) Box 1, (b) Box 2 and (c) Box 3. The sign of the transports is changed as to maintain the same sign convention in all boxes: positive mass transports flow out of the box and negative mass transports flow into the box.

The inverse box model (Wunsch, 1978, 1996) uses constraints on transports to adjust the reference velocities and produce a consistent solution for each enclosed region, reducing the large initial imbalances. The following equation for mass transport is solved:

$$\iint \rho b dx dz = -\iint \rho v_r dx dz + E_k$$

where ρ is the seawater density, b designates the unknown reference velocity, v_r is the initial estimate for the geostrophic velocity derived from the thermal wind equation and after incorporating the reference velocities through an adjustment to the SADCP or LADCP data, E_k is the normal Ekman transport to the section, and the along-section and vertical coordinates are denoted by x and z, respectively. Appendix A provides the full matrix equation and its derivation, while the constraints used are given in Table 1.

Table 1. Constraints and results of the inverse model for the South Atlantic Ocean as obtained using the 34.5ºS, 24ºS and 10ºW sections. Positive transports are northward-eastward, and negative are southward-westward; while in the box imbalances, positive/negative values represent divergence/convergence. Initial and final transports relative to the reference layer (at γ^n=28.15 kg/m^3 for the 34.5ºS section and γ^n=27.84 kg/m^3 for the 24ºS and 10ºW sections) are listed. The constraints set in the inverse model for the regional transports are also shown; NC stands for non-constraint.

South Atlantic Ocean	Property	Longitude	Layers	Constraint (Sv)	Initial (Sv)	Final (Sv)
A10.5 – 34.5ºS	Bering imbalance[a]	All	All	-0.8 ± 0.6	-0.5	-0.7 ± 2.9
	Vema Channel[b]	50.8ºW to 34.9ºW	9:11	4.0 ± 0.4	6.5	4.0 ± 0.9
	Hunter Channel[c]	33.6ºW to 27.0ºW	9:11	2.9 ± 1.2	-0.7	2.8 ± 1.0
	Brazil Current[d]	Coast to 49.2ºW	1:5	-14.0 ± 8.8	-20.0	-16.5 ± 1.3
	Benguela Current[e]	10.9ºE to coast	1:5	24.0 ± 17.0	27.5	26.3 ± 2.0
	DEBC[e]	13.6ºE to coast	6:9	-12.0 ± 17.0	-8.3	-15.1 ± 3.5
	DWBC[f]	Coast to 47.3ºW	6:9	-15.0 ± 23.0	-18.7	-13.9 ± 3.0
	$DWBC_{rec}$	47.3ºW to 46.8ºW	6:9	NC	3.3	3.0 ± 1.3
A09.5 – 24ºS	Bering imbalance[a]	All	All	-0.8 ± 0.6	4.8	-0.7 ± 3.1
	Walvis R. North[g]	4.6ºE to coast	9:11	0.0 ± 1.0	5.0	-0.7 ± 0.7
	Brazil Current[h]	Coast to 40.5ºW	1:5	-8.4 ± 5.0	-8.4	-7.3 ± 0.9
	Benguela Current	27.6ºW to coast	1:5	NC	25.8	21.2 ± 1.8
	DEBC	2.6ºE to coast	6:9	NC	-3.5	-16.3 ± 4.7
	DWBC	Coast to 35.2ºW	6:9	NC	-9.2	-8.7 ± 3.8
	$DWBC_{rec}$	35.2ºW to 33.7ºW	6:9	NC	6.5	6.4 ± 2.7
34.5ºS (West) – 10ºW – 24ºS (East)	Bering imbalance[a]	Coast to 10.6ºW (34.5ºS) All (10ºW) 9.9ºW to coast (24ºS)	All	-0.8 ± 0.6	22.7	-0.9 ± 11.0
24ºS (West) – 10ºW – 34.5ºS (East)	Bering imbalance[a]	Coast to 10.4ºW (24ºS) All (10ºW) 10.0ºW to coast (34.5ºS)	All	-0.8 ± 0.6	29.9	-1.9 ± 9.4
34.5ºS – 24ºS	Total mass conserved in Box 1	All (34.5ºS) All (24ºS)	All	0.0 ± 1.0	5.3	0.0 ± 15.5
34.5ºS (West) - 10ºW - 24ºS (West)	Total mass conserved in Box 2	Coast to 10.4ºW (34.5ºS) All (10ºW) Coast to 10.6ºW (24ºS)	All	0.0 ± 1.0	30.4	1.2 ± 10.2
34.5ºS (East) – 10ºW – 24ºS (East)	Total mass conserved in Box 3	10.0ºW to coast (34.5ºS) All (10ºW) 9.9ºW to coast (24ºS)	All	0.0 ± 1.0	-25.0	-1.2 ± 12.6

[a] Bering imbalance in Total Mass Conservation from Coachman & Aagaard (1988).
[b] Bottom transport constraint in the Vema Channel from Hogg et al. (1982).
[c] Bottom transport constraint in the Hunter Channel from Zenk et al. (1999).
[d] Brazil Current constraint from Chidichimo et al. (2021).
[e] Benguela Current and Deep Eastern Boundary Current (DEBC) constraints from Kersalé et al. (2019).
[f] Deep Western Boundary Current (DWBC) constraint from Meinen et al. (2017).
[g] Bathymetric constraint from Warren & Speer (1991).
[h] Boundary current constraints from cruise-based ADCP profiles.

The approach used for the inverse model solution is the same approach as the one developed by Joyce et al. (2001) and later applied by Arumí-Planas et al. (2022), Casanova-Masjoan et al. (2020) and Hernández-Guerra et al. (2014). The unknown geostrophic reference velocity at each station pair, as well as the section adjustment to the Ekman velocity, along with their standard deviations, are estimated using a system of mass conservation equations, which requires an enclosed region. This procedure provides forty-eight equations for the vertically integrated mass constraints with 262 unknowns (the total number of station pairs of the three hydrographic sections combined). For each box, both total mass and mass in each neutral density layer are conserved, with the Ekman transport adjustment included in the first layer. The next four constraints are the mass balance (based on the Bering Strait transport) for sections 24ºS and 34.5ºS separately, as well as mass balance for two transatlantic sections composed of the western/eastern station pairs section 24ºS plus section 10ºW and the eastern/western station pairs of section 34.5ºS, respectively. In addition to the total mass constraints, eight regional constraints across several longitude and depth ranges were introduced to reduce this underdetermined system (Table 1). These constraints have been previously applied in earlier studies of the South Atlantic Ocean as in other inverse models (Table 1; Hogg et al., 1982; Warren & Speer, 1991; Zenk et al., 1999), although the recent study of Finucane & Hautala (2022) suggested that the bottom transport estimated in the Hunter Channel by Zenk et al. (1999) could be overestimated. We have also included new constraints for 34.5ºS from recent studies by Chidichimo et al. (2021), Kersalé et al. (2019) and Meinen et al. (2017) using data from the moored arrays deployed along this section as part of the South Atlantic MOC Basin-wide Array (SAMBA) (Ansorge et al., 2014; Garzoli & Matano, 2011; Meinen et al., 2013, 2017, 2018). Moreover, we use ADCP data from section 24ºS to constrain the Brazil Current (as previously done for the hydrographic section at 30ºS by Hernández-Guerra et al. (2019).

The Gauss-Markov method is used to solve the inverse problem (Wunsch, 1996), which requires *a priori* variances for each equation and solution. The *a priori* variances for each equation, corresponding to each regional constraint, are expressed as standard deviations (Table 1), except the Brazil Current at 24ºS where we have assigned 5 Sv to consider the uncertainty of the Brazil Current transport based on the differences between hydrographic sections at 24ºS in 2009 (Bryden et al., 2011) and 2018, as also considered in Hernández-Guerra et al. (2019) for a 30ºS section. Furthermore, we have assigned *a priori* variances for the layer mass conservation equations: 3.6 Sv in each of layers 1-4, 2.2 Sv for layers 5-7, and 1.1 Sv for layers 8-11. The *a priori* velocity variance for the ocean interior's solution is set to $(2\ cm/s)^2$, while it is raised to $(4\ cm/s)^2$ in regions with strong shear, which corresponds to both eastern and western boundaries. The *a priori* variances are large enough to adjust the mass transports for every oceanographic cruise condition with the inverse model (Table 1). The Gauss-Markov method solves the underdetermined system of equations by selecting the solution with the least variance, given the reference level velocities along with their corresponding uncertainties. Finally, we compute the adjusted mass transports and their uncertainties.

The initially adjusted velocities estimated at the reference level, those from the SADCP and LADCP data, and as produced by the inverse model are shown in Figure 5. The velocities adjusted using the ADCP data (Fig. 5a) are greater than those obtained from the inverse model (Fig. 5b). The inverse solution velocities are not significantly different from zero (i.e., -0.02 ± 0.08 cm/s) in most ocean interior stations, as in earlier inverse models (Arumí-Planas et al., 2022; Hernández-Guerra & Talley, 2016; Hernández-Guerra et al., 2019), as well as on the eastern and western boundaries (i.e., -0.04 ± 0.08 cm/s). The inverse model adjustment does not produce a significant change to initial Ekman transports on any section (inverse estimates of -1.6 ± 0.2 Sv at 24ºS, 0.1 ± 0.2 Sv at 34.5ºS, and 0.1 ± 0.1 Sv at 10ºW).

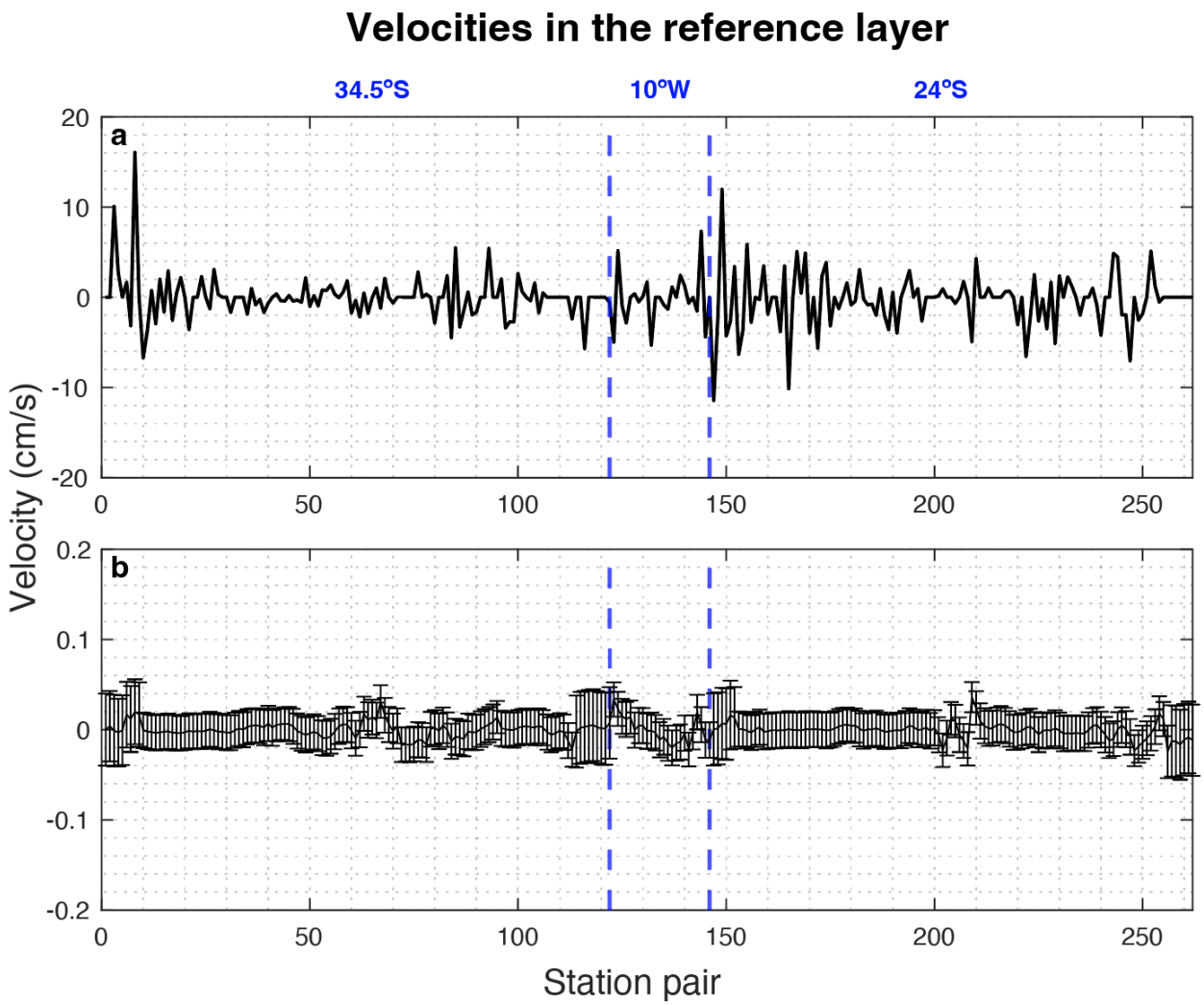

Fig. 5. (a) Reference velocities (cm/s) as adjusted using ADCP data and (b) velocity adjustment from the inverse model with error bars as a function of station pair numbers for the three hydrographic sections: 34.5ºS (station pair from 1 to 122), 10ºW (stations pair from 123 to 146), and 24ºS (station pair from 147 to 262). The blue dotted lines separate the transect, as shown in the upper legend. Positive and negative velocities are north/east or south/west, respectively.

5. Adjusted Meridional and Zonal Transports

After applying the inverse model, the final adjusted mass transports per neutral density layer in each enclosed region model are presented in Figure 6. The total mass imbalance in each closed box is insignificantly different from zero, well within the corresponding uncertainties (0.0±15.5 Sv in Box 1, 1.2±10.2 Sv in Box 2, and -1.2±12.6 in Box 3). Therefore, we may say that mass transport is conserved in all three closed regions.

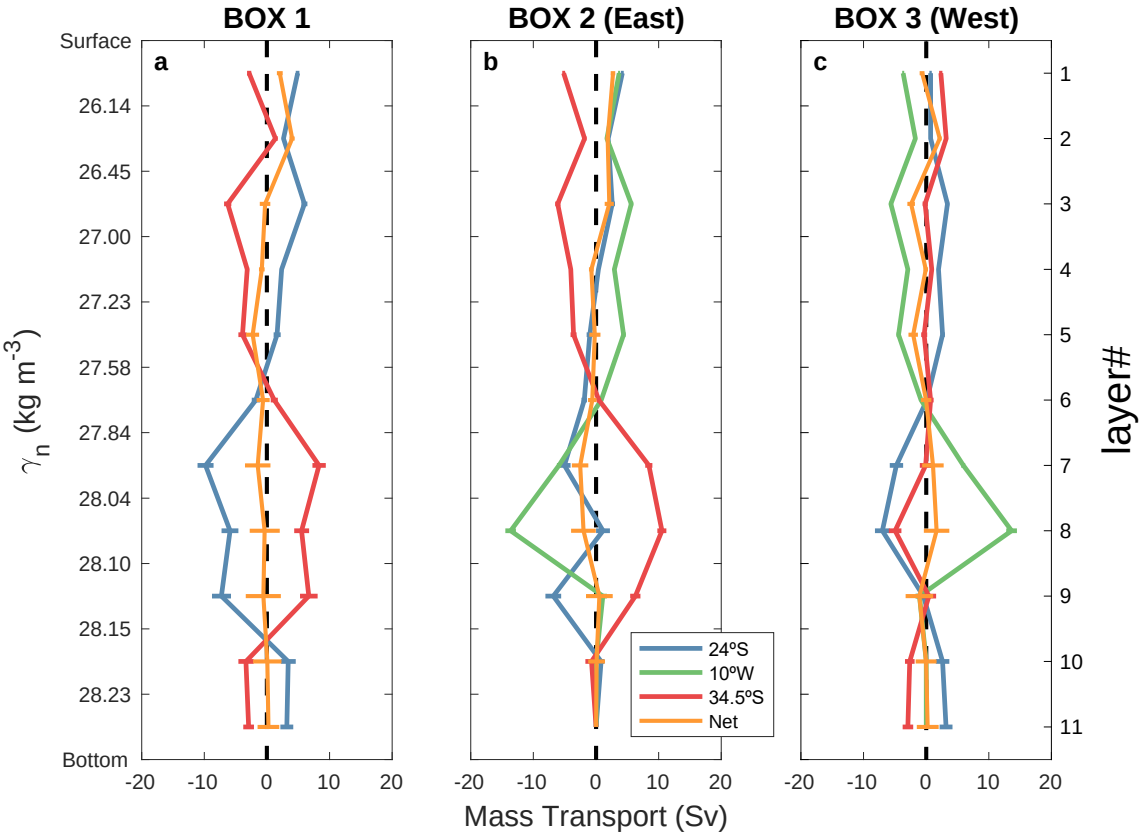

Fig. 6. Final integrated mass transports (Sv) per neutral density layer at 24ºS (blue line), 10ºW (green line), 34.5ºS (red line) and the net (orange line) with the corresponding error bars, in the South Atlantic Ocean; the net imbalance per layer is also shown. The three panels correspond to the mass transport in (a) Box 1, (b) Box 2 and (c) Box 3. The sign of the transports is changed as to maintain the same sign convection in all boxes: positive mass transports flow out of the box and negative mass transports flow into the box.

The meridional overturning transports across the transatlantic sections at 34.5ºS and 24ºS are computed by zonally and vertically integrating the mass transport from the bottom to the sea surface (Fig. 7). The strength of the AMOC at each latitude is defined as the vertical maximum of the stream function, which is always found in the upper cell (Buckley & Marshall, 2016). The AMOC intensity at 24ºS is 17.5±0.9 Sv, which is stronger than the 14.8±1.0 Sv estimated at 34.5ºS. Based on Fig. 7, we may divide the Atlantic Ocean in a three-layer system at 24ºS and 34.5ºS, with mass transports flowing northward in the uppermost layers (1-5), southward in the deep layers (6-9), and northward in the abyssal layers (10-11); it is the upper cell that differs most between 24ºS and 34.5ºS. In contrast, in the meridional 10ºW section (not shown) there is no mass transport in the abyssal layers (Fig. 6b and c), hence it can be viewed as a two-layer system, with mass transports flowing westward in the uppermost layers (1-5) and eastward in the deep layers (6-9).

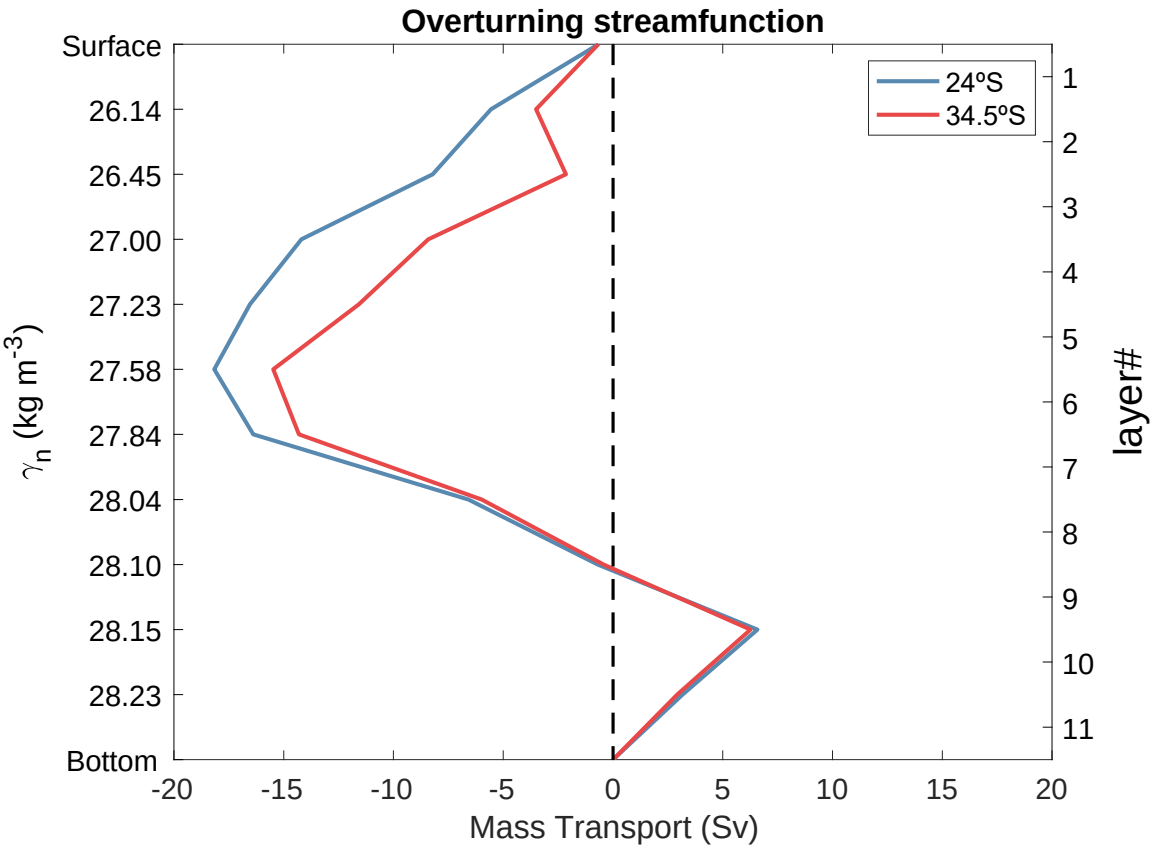

Fig. 7. Overturning stream function of mass transport across 24ºS (red line) and 34.5ºS (blue line) in the Atlantic Ocean for 2018 and 2017, respectively. The function is computed by integrating the mass transport vertically and horizontally in isoneutral layers, from the seafloor to the sea surface across the entire section.

6. Horizontal Circulation from Adjusted Transport

Figure 8 presents the horizontally accumulated mass transport for different isoneutral layers along 24ºS (a, b, c), 34.5ºS (d, e, f), and 10ºW (g, h). The inverse model results are presented with positive northward/eastward transports and negative southward/westward transports. For sections 24ºS and 34.5ºS, the mass transport is accumulated integrating eastward, whilst for section 10ºW, it is accumulated integrating northward. As the inverse box solution finds a solution that satisfies mean constraints and uses hydrographic data from different years, they represent in some sense a time mean circulation. For this reason, we have included in Figure 8 the accumulated transports using ECCO (2017) and GLORYS (2017-2019) to examine averages over the time period from both models for 24ºS and 34.5ºS sections, and none for 10ºW because no models are available for 2021.

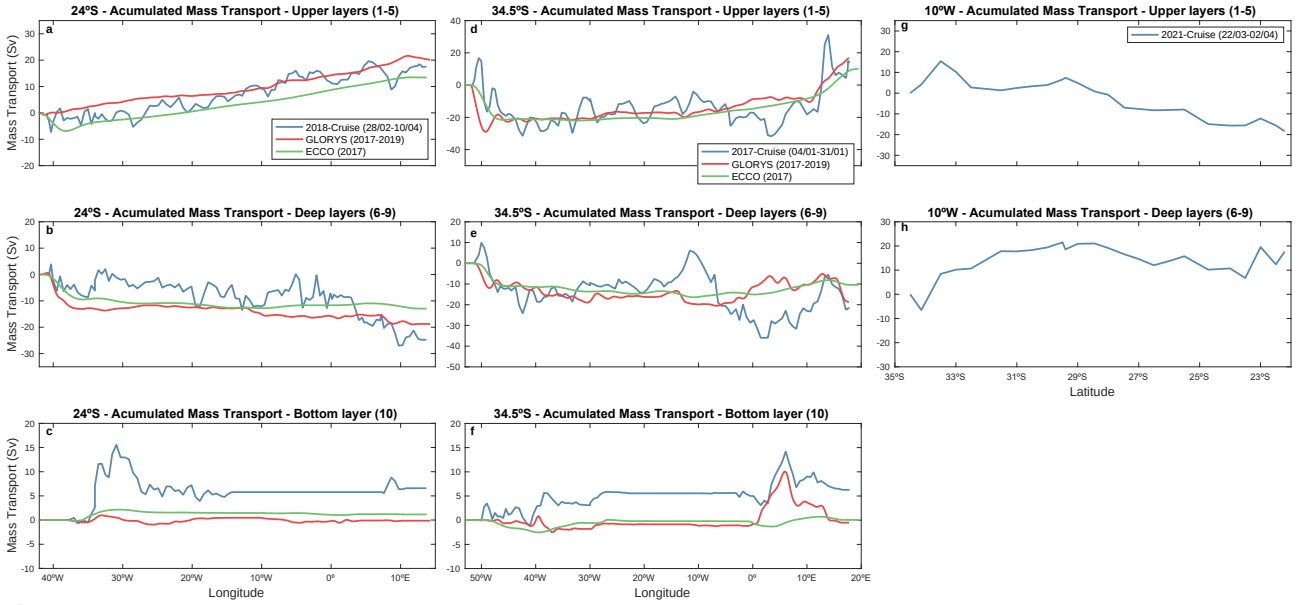

Fig. 8. Eastward accumulated mass transports (Sv) at 24ºS (a,b,c) and 34.5ºS (d,e,f), and northward accumulated mass transport (Sv) at 10ºW (g,h) in the Atlantic Ocean for the upper (1:5), deep (6:9), and bottom (10:11) layers; the positive/negative mass transports are northward/southward at 24ºS and 34.5ºS, and eastward/westward at 10ºW. The mass transports obtained from the inverse model (blue curves) are compared with the available simulations from the ECCO (green curves) and GLORYS (red curves) circulation models averaged over time.

6.1 Upper ocean

The SACW-AAIW stratum includes the thermocline and intermediate waters (from the sea surface down to γ^n = 27.23 kg/m^3, approximately down to 730 m; Figures 8a, d, g). The mass transport in these upper layers presents a northward recirculation near the western boundary, a net northward mass transport through the ocean interior, and a wide and slow Benguela Current in the eastern boundary, rendering the typical pattern of the subtropical gyre (Fig. 8a and d). The alternating mass transports in the entire subtropical gyre are caused by mesoscale eddies, bringing the saw-like streamfunction described in Hernández-Guerra et al. (2005).

In the western boundary, off the east coast of South America, a relatively strong Brazil Current flows poleward. The Brazil Current has been previously described by Garzoli et al. (2013) from XBTs at 35ºS, by Müller et al. (1998) from current moorings between 20ºS and 28ºS, and by McDonagh & King (2005) and Hernández-Guerra et al. (2019) from hydrographic data at 30ºS. In our study, the Brazil Current shows up clearly by the tilting isopycnals, at 24ºS as a narrow jet (≈ 37 km) from the coast to about 40.5ºW with a southward mass transport of -7.3±0.9 Sv at 24ºS, and at 34.5ºS as a much wider jet that extends from the coast to about 49.2ºW (127 km) with a southward transport of -16.6±1.3 Sv (see also Manta et al., 2020) (Table 1). Thus, the Brazil Current increases its mass transport to the south. In these upper layers, the OGCM reproduces reasonably well the inverse model transports at 24ºS and 34.5ºS (Fig. 8a and d, respectively), but with some significant differences in the extension and intensity of the boundary transports. Specifically, at 24ºS GLORYS do not show a western boundary current, while ECCO presents a similar Brazil Current transport of -6.8±1.5 Sv from the coast to 38.3ºW. The OGCM transports at 34.5ºS are stronger (-28.7±12.7 Sv from the coast to 49.3ºW in GLORYS and -21.5±1.9 Sv from the coast to 46.5ºW) than the inverse model.

In the eastern margin, between the African coast to about 10.9ºE (Reid, 1989), the Benguela Current is observed as a relatively wide and strong northward eastern boundary current of the South Atlantic Subtropical Gyre. The Benguela Current flows northward becoming wider at 24ºS (from 27.6ºW to the coast). The strength of the Benguela Current, from above ~730 m depth (layers 1 to 5, between the surface and γ^n = 27.23 kg/m^3), is estimated to be 26.4±2.0 Sv at 34.5ºS, which is slightly stronger than the much wider Benguela Current of 21.2±1.8 Sv at 24ºS (Table 1). The mass transport at 10ºW, between 28.4º and 22.4ºS, is –19.2±1.4 Sv, which corresponds to the branch of the Benguela Current that runs above the MAR (Fig. 8g). At 24ºS, GLORYS and ECCO represent a weaker Benguela Current in the western boundary of 14.6±2.7 and 15.3±0.8 Sv,

respectively, from 27ºW to the coast. Furthermore, at 34.5ºS OGCM presents a similar Benguela Current transport to the hydrographic data from 9.3ºE to the coast of 26.9±14.1 Sv and from 8.5ºE to the coast of 28.1±0.7 Sv in GLORYS and ECCO, respectively.

6.2 Deep layers

The mass transport for the UCDW-NADW deep layers flows southward and eastward (layers 6 to 9, from 27.58 kg/m^3 to 28.1 kg/m^3) (Figs. 8b, e, h). The accumulated poleward mass transport in these layers presents no significant differences through 24ºS (-24.7±2.5 Sv) and 34.5ºS (-21.7±2.2 Sv). Moreover, the accumulated mass transport for these layers at 10ºW presents a net mass transport of 17.7±1.1 Sv, which reflects that part of the deep waters flow eastward from 34.5ºS to 33.5ºS (10.2±2.8 Sv) before recirculating in the south, an eastward flow close to 24ºS (7.5±4.4 Sv), and other recirculation routes along the meridional section (Fig. 8h).

According to multiple research studies (e.g., Ganachaud, 2003; Meinen & Garzoli, 2014; Meinen et al., 2017; Müller et al., 1998), NADW is principally transported southward in the Atlantic Ocean by the DWBC. Based on the hydrographic sections examined in the present study, the DWBC presents a southward mass transport of -8.7±3.8 Sv from the coast to 35.2ºW at 24ºS and -13.9±3.0 Sv from the coast to 47.3ºW at 34.5ºS (Table 1). The northward recirculation of the DWBC is found just east of these longitudes (to about 33.7ºW and 46.8ºW at 24ºS and 34.5ºS, respectively), presenting an equatorward mass transport of 6.4±2.7 Sv at 24ºS and 3.0±1.3 Sv at 34.5ºS (Table 1). In the deep layers, at 24ºS GLORYS presents a stronger DWBC poleward mass transport (-13.0±3.8 v) than the inverse model (Fig. 8b), while ECCO presents a similar DWBC of -9.4±2.6 Sv both from the coast to 35.8ºW. At 34.5ºS, the OGCM replicates fairly well the intense DWBC (-11.7±7.4 Sv from the coast to 48.5ºW in GLORYS, and -11.1±1.6 Sv from the coast to 46ºW in ECCO). However, both numerical models have substantial differences from the inverse model in the ocean interior (Fig. 8e). These differences could be explained by the fact that our inverse model results present higher resolution because they are based on observations. In contrast, OGCMs often use assumptions and parameterizations to simplify the complexity of ocean processes, introducing errors and biases into the model results, particularly in the ocean interior and deep layers where observational data are limited.

From our inverse model results, the DEBC presents a northward mass transport of -16.3 ± 4.7 Sv at 24ºS, which is similar to the -15.1 ± 3.5 Sv obtained at 34.5ºS. Therefore, the branch from the DWBC feeding the DEBC comes from latitudes north of 24ºS, which is corroborated with the westward flow above the MAR close to 24ºS at 10ºW. At 24ºS in the eastern boundary, GLORYS (-3.0±3.3 Sv from 3.8ºE to the coast) and ECCO (-1.8±1.8 Sv from 7.3ºE to the coast) present a weaker DEBC than the inverse model, and at 34.5ºS ECCO also displays a weaker DEBC of -2.3±0.5 Sv from 14ºE to the coast, while GLORYS estimates a similar transport (-13.5±12.7 Sv from 12.8ºE to the coast) if compared with the inverse model.

6.3 Bottom layers

The LCDW-AABW water masses (layers 10-11, below γ^n=28.15 kg/m^3) present a low net equatorward mass transport of 6.6±1.6 Sv at 24ºS and 6.3±1.5 Sv at 34.5ºS (Figures 8c, f). In the western basin, the northward transport over the Argentine Basin at 34.5ºS (5.6±1.1 Sv) passes through the Vema Chanel (3.5±0.7 Sv) and Hunter Channel (2.3±0.9 Sv) to reach 24ºS (5.8±1.5 Sv). Whereas in the eastern basin, the equatorward flow over the Cape Basin at 34.5ºS (8.6 ± 3.5 Sv) barely reaches 24ºS (3.0±0.8 Sv), as some flow recirculates (2.2±0.7 Sv) and some flow turns back to 34.5ºS (-7.9±3.6 Sv). Additionally, the MAR limits the east/westward flow of the abyssal waters at 10ºW, presenting no mass transport in these layers. At 24ºS, GLORYS shows no mass transport in the abyssal layers (Fig. 8c) but does fairly well at 34.5ºS, reproducing the alternating mass transport between both basins, while the ECCO output differs greatly from the inverse results at both latitudes.

7. Heat and Freshwater Transports

The heat transport is computed by using the following expression:

$$HT = \sum_i \sum_j \rho_{ij} c_{p_{ij}} \theta_{ij} v_{ij} \Delta x \Delta z$$

where ρ_{ij} is the density, $c_{p_{ij}}$ is the heat capacity of the seawater, θ_{ij} is the potential temperature, and v_{ij} is the absolute cross-section velocity, and the i,j subindexes identify the station pair and layer, respectively. Positive values indicate a northward heat flux, while negative values imply a southward heat flux.

The positive values estimated from the meridional heat transports after the inverse model at 34.5ºS (0.30±0.05 PW) and 24ºS (0.80±0.05 PW) indicate an increase in the equatorward flux in the subtropical South Atlantic. In addition, these results reflect the northward direction of the warm waters in the upper layers at both latitudes in the South Atlantic Ocean. The heat transport in GLORYS agrees with the inverse model results at these latitudes (0.43±0.26 PW and 0.71±0.14 PW at 24ºS and 34.5ºS, respectively), while ECCO presents a similar heat transport at 34.5ºS (0.34±0.15 PW) and weaker at 24ºS of 0.44±0.10 PW than our inverse model results at this latitude but yet reproduces the increase in northward heat transport.

The freshwater flux (in FSv, Sverdrup for freshwater transport without mass balance) is estimated according to Joyce et al. (2001), taking into account the precipitation over evaporation:

$$\bar{F} = -\sum_{i}\sum_{j} T_{ij} S'_{ij} / S_0$$

where T_{ij} is the absolute mass transport, S'_{ij} is the anomaly of salinity (Salinity-S_0), both in layer i at station pair j, and S_0 is the global ocean mean salinity set to 34.9 as in Arumí-Planas et al. (2022), Hernández-Guerra & Talley. (2016) and Talley (2008). At 24ºS there is a southward transport of freshwater (-0.07±0.02 FSv), while at 34.5ºS there is a northward transport of freshwater (0.18±0.02 FSv). Therefore, our results suggest that in the 24ºS-34.5ºS domain, evaporation predominates over precipitation (as in Caínzos et al., 2022). The freshwater transports from the OGCM and the inverse model are not significantly different. The GLORYS freshwater transports have the same direction as the inverse model at 24ºS (-0.05±0.07 FSv) and 34.5ºS (0.25±0.11 FSv), while ECCO presents a slightly higher value at 24ºS (0.01±0.05 FSv) and weaker freshwater transport at 34.5ºS (0.07±0.07 FSv) than the inverse model.

8. South Atlantic Schematic Circulation

Figure 9 sketches a circulation in the upper, deep and bottom layers in the South Atlantic between 24ºS and 34.5ºS and above the MAR that is coherent with the mass transports as inferred from our inverse box model. The net mass transport from the inverse model indicates that the predominant northward path of the upper layers is found in the easternmost region of the 34.5ºS section (26.3±2.0 Sv), expanding to a wider area at 24ºS (8.1±0.7 Sv east of the 10ºW). It also shows that a fraction of the northward flow turns west through the MAR in the northern stations of 10ºW, between 22.4ºS and 28.4ºS (-19.2±1.4 Sv), which then splits into two branches, one flowing north to 24ºS (13.1±1.6 Sv west of 10ºW, summing a total northward flow of 21.2±1.8 Sv at 24ºS) and the second branch reaching the western boundary (6.1±1.4 Sv). These mass transports together with the southward flow at the westernmost part of the 24ºS section to 34.5ºS describe the anticyclonic course of the South Atlantic subtropical gyre.

In the deep layers, the DWBC and DEBC flow southward from 24ºS (-8.7±3.8 Sv and -16.3±4.7 Sv, respectively) to 34.5ºS (-13.9 ± 3.3 Sv and -15.1±3.5 Sv, respectively). The scheme turns more complicated as an eastward branch flows over the MAR (7.5 ± 4.4 Sv) near 24ºS and several recirculation routes appear to take place throughout the entire 10ºW section (Fig. 8).

Finally, the abyssal waters present a northward mass transport from the Argentine Basin (5.6±1.1 Sv at 34.5ºS) to the Brazil Basin (5.8±1.5 Sv at 24ºS), as well as an equatorward flow from the Cape Basin (8.6±3.5 Sv at 34.5ºS), which barely reaches the 24ºS (3.0±0.8 Sv) section before returning southwards (-2.2±0.7 Sv) until 34.5ºS (-7.9±3.6 Sv).

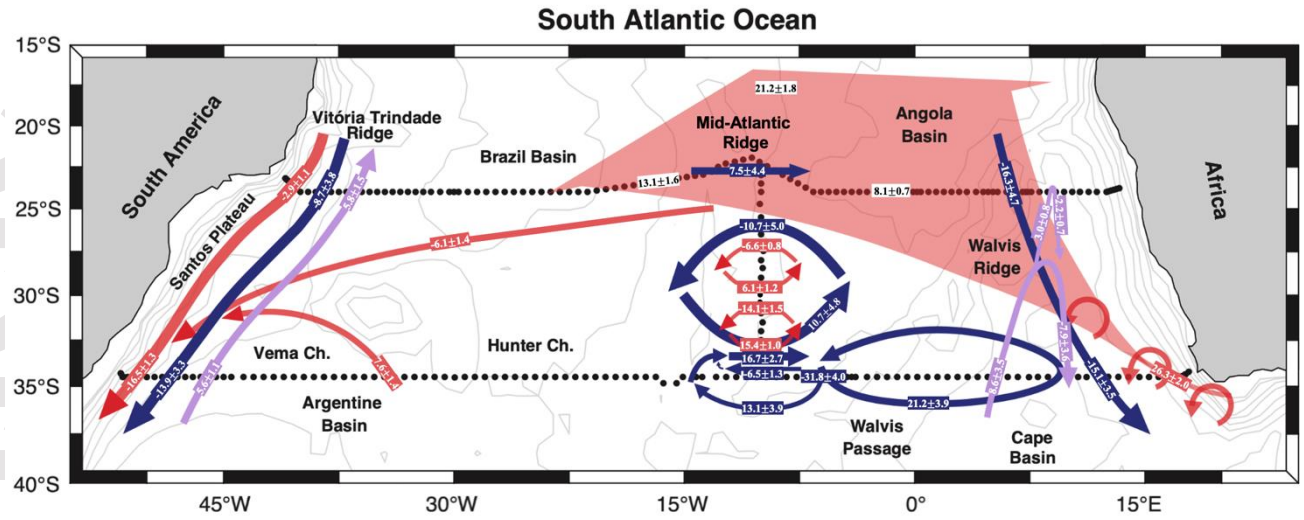

Fig. 9. Schematic circulation in the upper (red), deep (blue) and bottom (purple) layers of the South Atlantic Ocean, consistent with the mass transports calculated across 24ºS, 10ºW and 34.5ºS. The net mass transports (in Sv) are indicated, with the positive transports northward and eastward and the negative transports southward and westward.

9. Discussion and Concluding Remarks

We have used hydrographic data sampling three enclosed regions for inverse modelling in the South Atlantic subtropical gyre. The initial geostrophic velocity is firstly adjusted to the velocities from ADCP data, and subsequently with the reference velocities as obtained from an inverse box model, such as to satisfy water mass balances in the three enclosed regions.

In the upper layers, the Brazil Current flows as a relatively intense western boundary current, increasing southward from -7.3±0.9 Sv at 24ºS to -16.6±1.3 Sv at 34.5ºS. The GLORYS and ECCO models do not properly represent the Brazil Current at 24ºS, but both represent a slightly weaker (GLORYS: -12.7 Sv in January; ECCO -9.8 Sv in 2017 mean) or stronger (GLORYS -29.1 Sv in 2017-2019 mean; ECCO -22.5 Sv in January) Brazil Current transport at 34.5ºS. Our result at 24ºS agrees with the 4.9 to 12.3 Sv estimated by Bryden et al. (2011) but is slightly higher than the 5.8±0.1 Sv estimated by Evans et al. (2017). Further, our estimates for the Brazil Current are consistent with a recirculation cell south of 28ºS in the western South Atlantic, found both by Stramma (1989) (from -9.6 Sv at 24ºS to -17.5 Sv at 33ºS) and by Garzoli et al. (2013) (from -8.6±4.1 Sv at 24ºS to -19.4±4.3 Sv at 35ºS). Moreover, Schmid & Majumder (2018) combined Argo-float and sea surface height data to propose that the Brazil Current intensifies to the south, but with weaker mean mass transports (-2.3±0.9 at 24ºS and -12.6±2.6 Sv at 35ºS).

The Benguela Current flows in the upper layers as a broad and relatively strong equatorward eastern boundary current, which changes from 26.4±2.0 Sv at 34.5ºS to 21.2±1.8 Sv at 24ºS. The GLORYS and ECCO models present a similar transport at 34.5ºS, of 21.6 Sv and 20.3 Sv, respectively, and GLORYS shows a Benguela Current of 25.5 Sv at 24ºS. Our transports at 34.5ºS agree with the previously reported values by Kersalé et al. (2019) (24.0±17.0), Garzoli et al. (2013) (22.5±4.7 Sv) and Majumder & Schmid (2018) (19±3 Sv). These results show that the Benguela Current is a relatively strong eastern boundary current, much stronger than the Canary Current in the North Atlantic (Casanova-Masjoan et al., 2020) and the Peru-Chile Current in the South Pacific (Arumí-Planas et al., 2022). The accumulated mass transport at 10ºW presents a westward mass transport in the upper layers (-18.4±0.4 Sv), consistent with the westward branch of the Benguela Current over the MAR (Garzoli & Gordon, 1996; Richardson & Garzoli, 2003; Rodrigues et al., 2007; Stramma, 1991).

The accumulated mass transport in the deep layers presents a net northward mass transport of UCDW-NADW through 24ºS and 34.5ºS of -24.7±2.5 Sv and -21.7±2.2 Sv, respectively. In the western boundary, the deep waters are transported southwards by the DWBC, which presents a southward mass transport of -8.7±3.8 Sv at 24ºS and -13.9±3.0 Sv at 34.5ºS. At 24ºS, the GLORYS output presents a stronger DWBC poleward mass transport (-19.1 Sv) than the inverse model. While at 34.5ºS, neither of the two ocean models properly represents

the interior circulation in the deep layers, but both display the intense poleward DWBC (-13.4 Sv in GLORYS and -13.2 Sv in ECCO). Adjacent to the DWBC, we find a northward transport of 6.4±2.7 Sv at 24ºS and 3.0±1.3 Sv at 34.5ºS. Further, the interior NADW pathway, which originates close to the Vitória-Trindade Ridge at about 20ºS, extends eastward crossing the MAR between 20º and 25ºS (Arhan et al., 2003; Garzoli et al., 2015; Speer et al., 1995; van Sebille et al., 2012), then it moves to the Cape Basin and flows southward across the African continental slope as a DEBC (Arhan et al., 2003; Palma & Matano, 2017; Stramma & England, 1999). In the eastern boundary, the deep waters are transported southward by the DEBC (-16.3±4.7 Sv at 24ºS and -15.1±3.5 Sv at 34.5ºS). For comparison, at 24ºS, GLORYS presents a weaker DEBC (-6.8 Sv) than the inverse model, while at 34.5ºS both GLORYS and ECCO have weaker transports than the inverse model (-6.0 Sv and 1.4 Sv, respectively). At 10ºW, the deep layers display a net eastward transport of 17.7 ± 1.1 Sv, with some 10 Sv recirculating between the eastern and western basins. An eastward transport is found close to 24ºS (7.5±4.4 Sv), reflecting the NADW pathway into the eastern basin between 20ºS and 25ºS previously described by Arhan et al. (2003) and Reid (1989).

In this study, we find a northward heat transport in the subtropical South Atlantic, both at 34.5ºS (0.30±0.05 PW) and 24ºS (0.80±0.05 PW), which reflects the equatorward mass transport in the warm upper layers. The northward heat transport in GLORYS is similar to our estimate at both latitudes (0.43±0.26 PW and 0.71±0.14 PW at 24ºS and 34.5ºS, respectively), while the heat transport in ECCO is similar at 34.5ºS (0.34±0.15 PW) but weaker at 24ºS (0.44±0.10 PW) than our inverse model results. The heat transport estimated at 34.5ºS agrees with the 0.27±0.10 PW estimated by Manta et al. (2020) using the same hydrographic section, the 0.49±0.23 PW from altimetry data computed by Dong et al. (2015), the 0.5±0.2 PW from acoustic inversion reported by Kersalé et al. (2021), as well as with the 0.42±0.18 PW from numerical model data obtained by Perez et al. (2011). In the same way, our result at 24ºS presents no significant differences from previous estimations with hydrographic data - 0.64±0.18 PW (Fu, 1981) and 0.7±0.1 PW (Bryden et al., 2011) - but is higher values than the 0.4±0.1 PW estimated by Evans et al. (2017) and slightly higher than the 0.66±0.07 PW reported by Caínzos et al. (2022). Some of these differences are likely the result of the differences in years and months when the cruises were carried out (Caínzos et al., 2022).

The negative freshwater flux at 24ºS (-0.07±0.02 FSv) and the positive freshwater transport at 34.5ºS (0.18±0.02 FSv) indicate a convergence of freshwater in the 24ºS-34.5ºS domain, pointing out that this is a region where evaporation predominates over precipitation. The freshwater transports from GLORYS present no significantly different values from the inverse model at both latitudes (-0.05±0.07 FSv and 0.25±0.11 FSv at 24ºS and 34.5ºS, respectively), while ECCO presents slightly higher (0.01±0.05 FSv at 24ºS) and weaker (0.07±0.07 FSv at 34.5ºS) freshwater transports than the inverse model. Our result at 24ºS agrees with the weak northward freshwater transport (0.01±0.09 FSv) obtained by Caínzos et al. (2022) using WOCE and GO-SHIP data for the period 2010-2019. The freshwater flux obtained at 34.5ºS is moderately lower than the freshwater transport of 0.23±0.02 Sv obtained by (Manta et al., 2021) at this same latitude.

The comparison of the circulation patterns as deduced from the inverse model with two different OGCM (ECCO and GLORYS) suggests that these ocean models are useful to study these sections in the upper layers (γ^n< 27.58 kg/m^3, 1140 m depth) with some differences in the estimated boundary currents. However, the ECCO and GLORYS patterns of circulation in the deep and, especially, bottom layers (γ^n>27.58 kg/m^3) do not properly resemble the circulation pattern of the hydrographic data at 24ºS and 34.5ºS in the Atlantic Ocean. The comparison of the heat and freshwater transports from the inverse model with the OGCM suggests that ECCO presents noticeable differences from our results, but GLORYS can be useful for determining the direction and strength of these deep ocean fluxes.

Our inverse model results show an AMOC strength of 17.5±0.9 Sv at 24ºS and 14.8±1.0 Sv at 34.5ºS. The AMOC strength at 24ºS agrees fairly well with previous estimates at 24ºS by Evans et al. (2017) (20.2±2.0 Sv), and Bryden et al. (2011) (21.5/16.5 Sv in 2009/1983). Furthermore, our estimate of the AMOC strength at 34.5ºS agrees well with earlier estimates at this latitude, 15.6±1.4 Sv (Manta et al., 2021), 17.3±5.0 Sv (Kersalé et al., 2021), 14.7±8.3 Sv (Meinen et al., 2018), 15.6±3.1 Sv (Perez et al., 2011), and 18.1±2.3 Sv (Garzoli et al., 2013). However, it is weaker than transports obtained by Dong et al. (2015) and Majumder et al. (2016), 19.5±3.5 Sv and 20.7±4.1 Sv, respectively. The weaker upper AMOC strength and heat transport at 34.5ºS as

compared with 24ºS could be partly explained by the intense southward transport of the Brazil Current (-16.6±1.3 Sv at 34.5ºS and -7.3±0.9 Sv at 24ºS) during the period of this hydrographic cruise (Kersalé et al., 2019; Manta et al., 2021). Furthermore, mesoscale eddies also probably play a role in upper limb transport, as the mesoscale activity at 34.5ºS is higher than at 24ºS (Laxenaire et al., 2018).

Our inverse box model has provided a detailed view of the South Atlantic circulation by estimating the different ocean current transports at each layer set through 24ºS and 34.5ºS, as well as over the MAR between these two latitudes. The transports in the upper layers are consistent with the course of the subtropical South Atlantic anticyclonic gyre and the northwest route of the Benguela Current. The deep waters show the southward flow of the DWBC and DEBC, together with an eastward interbasin flow at the northern stations (close to 24ºS) of the 10ºW section, and different recirculation routes linking both basins. The abyssal layers exhibit northward mass transports through the Argentina and Cape basins, before the latest returns southward in the ocean interior, with no flow crossing above the MAR. Our results have also confirmed the characteristic northward heat transport across the subtropical South Atlantic Ocean, as well as the dominance of evaporation over precipitation.

Declaration of Competing Interest

The authors declare the following financial interests/personal relationships which may be considered as potential competing interests: Cristina Arumí-Planas reports financial support was provided by Agencia Canaria de Investigación, Innovación y Sociedad de la Información (ACIISI). Cristina Arumí-Planas reports a relationship with Agencia Canaria de Investigación, Innovación y Sociedad de la Información (ACIISI) that includes: employment.

Acknowledgments

This study was supported by the SAGA project (RTI2018-100844-B-C31, RTI2018-100844-B-C32 and RTI2018-100844-B-C33) funded by the Ministerio de Ciencia, Innovación y Universidades of the Spanish Government, and Feder. This article is a publication of the Unidad Océano y Clima from Universidad de Las Palmas de Gran Canaria, an R&D&I CSIC associate unit. The authors declare no competing interests. This work has been completed as part of C. Arumí-Planas's work at IOCAG, in the doctoral program in Oceanography and Global Change. C. Arumí-Planas acknowledges the Agencia Canaria de Investigación, Innovación y Sociedad de la Información (ACIISI) grant program of "Apoyo al personal investigador en formación" TESIS2021010028. The authors gratefully acknowledge the major efforts of the chief scientists who collected the hydrographic transects data: B. King, M. Emelianov, and J. Karstensen. Finally, the authors are grateful to M. Cubas-Armas for her help with the data analysis and representation.

Open Research

The wind data were collected from NCEP Reanalysis Derived data can be found at http://www.eslr.noaa.gov/psd/. Hydrographic data were collected from the Carbon Hydrographic Data Office (CCHDO) website in the frame of International WOCE and GO-SHIP projects (https://cchdo.ucsd.edu/). The hydrographic data at 34.5ºS were collected during the expedition of the German Research Vessel *Maria S. Merian* (MSM60) conducted in the summer of 2017 (Karstensen, 2020) can be found at https://doi.org/10.1594/PANGAEA.915898. The hydrographic data at 24ºS were collected as part of the Ocean Regulation of Climate by Heat and Carbon Sequestration and Transports (ORCHESTRA) program funded by the UK Natural Environment Research Council (NERC, grant number NE/N018095/1). ECCO data are available for download at https://ecco.jpl.nasa.gov/. GLORYS data are available for download at https://resources.marine.copernicus.eu/. The satellite altimetry data were collected from the Aviso database (http://las.aviso.oceanobs.com).

Appendix A

The absolute geostrophic velocity (v_a) for a given station pair, as a function of depth (z), is the summation of the relative velocity (v) and the velocity (b) at the reference level:

$$v_a(z) = v(z) + b$$

The inverse model finds the optimal solution for b at each station pair. Firstly, the mass conservation is applied

to the entire water column:

$$\iint \rho v_a dS = 0$$
$$\iint \rho(v+b)dS = 0 \qquad \text{(A.1a, b, c)}$$
$$\sum_{j=1}^{N}\sum_{q=1}^{Q}\rho_{jq}\left(v_{jq}+b_j\right)a_{jq} = 0$$

where the area integral dS is over the entire section area, a_{jq} is the area for each station pair j and isoneutral layer q. In (A.1) and the next equations, the term $\rho_{jq}v_{jq}$ is first summed over each 2 dbar interval within layer q. When mass transport is constrained to a particular non-zero value, M, (A.1c) becomes:

$$\sum_{j=1}^{N}\sum_{q=1}^{Q}\rho_{jq}\left(v_{jq}+b_j\right)a_{jq} = M \qquad \text{(A. 1d)}$$

where M is the mass transport constraint including the Bering Imbalance, and the limits for layers and station pairs are related to the constraint (Table 1). The total mass conservation is not exact because of the noise from eddies, internal waves, aliasing, measurements errors, etc.:

$$\sum_{j=1}^{N}\sum_{q=1}^{Q}\rho_{jq}b_j a_{jq} + n_{Total} = -\sum_{j=1}^{N}\sum_{q=1}^{Q}\rho_{jq}v_{jq}a_{jq} + M_{Total} \qquad \text{(A.2)}$$

where n_{Total} is the noise.

The following equations are obtained considering mass conservation in each layer q:

$$\sum_{j=1}^{N}\rho_{jq}b_j a_{jq} + n_q = -\sum_{j=1}^{N}\rho_{jq}v_{jq}a_{jq} + M_q \qquad q = 1,2,\dots,Q \qquad \text{(A.3)}$$

where M_q is the layer transport constraint and n_q is the layer noise. Next, this equation is written as:

$$\sum_{j=1}^{N} e_{jq}b_j + n_q = -y_q \qquad q = 1,2,\dots,Q \qquad \text{(A.4)}$$

where:

$$e_{jq} = \rho_{jq}a_{jq}$$
$$y_q = \sum_{j=1}^{N}\rho_{jq}v_{jq}a_{jq} - M_q \qquad \text{(A.5)}$$

The matrix equation is rewritten as:

Ab + n = -Y (A.6)

where **b** is a N x 1 vector of the unknowns (reference velocities and adjustment of the Ekman transport), **A** is a $(Q+1)$ x N matrix, **n** is a $(Q+1)$ x 1 vector, and **Y** is a $(Q+1)$ x 1 vector of values calculated from the CTD data and the externally imposed mass transports. (Q is for the equations for each layer and the +1 is the equation for conservation of the whole water column.)

The Ekman transport is included in the first layer, leading to the following system:

$$\begin{pmatrix} e_{11} & \cdots & e_{1n} & 1 \\ e_{21} & & e_{2n} & 0 \\ \vdots & \ddots & \vdots & \vdots \\ e_{q,1} & & e_{q,n} & 0 \\ e_{q+1,1} & \cdots & e_{q+1,n} & 1 \end{pmatrix} \begin{pmatrix} b_1 \\ \vdots \\ b_n \\ \Delta T_{Ek} \end{pmatrix} = \begin{pmatrix} y_1 + T_{Ek} \\ y_2 \\ \vdots \\ y_q \\ y_{q+1} + T_{Ek} \end{pmatrix}$$

To solve this matrix, the Gauss-Markov estimator is applied (Wunsch, 1996), as in Hernández-Guerra & Talley (2016).

For this inverse model, 15 different constraints are applied, corresponding to the mass conservation in each Box (three enclosed regions), plus 12 additional mass transport constraints based on previous studies of the boundary currents and deep flows (listed in Table 1).

10. References

Ansorge, I. J., Baringer, M. O., Campos, E. J. D., Dong, S., Fine, R. A., Garzoli, S. L., et al. (2014). Basin-Wide Oceanographic Array Bridges the South Atlantic. *Eos, Transactions American Geophysical Union*, *95*(6), 53–54. https://doi.org/10.1002/2014EO060001

Arhan, M., Mercier, H., & Park, Y.-H. (2003). On the deep water circulation of the eastern South Atlantic Ocean. *Deep Sea Research Part I: Oceanographic Research Papers*, *50*(7), 889–916.

https://doi.org/10.1016/S0967-0637(03)00072-4

Arumí-Planas, C., Hernández-Guerra, A., Caínzos, V., Vélez-Belchí, P., Farneti, R., Mazloff, M. R., et al. (2022). Variability in the meridional overturning circulation at 32°S in the Pacific Ocean diagnosed by inverse box models. *Progress in Oceanography*, *203*, 102780. https://doi.org/10.1016/j.pocean.2022.102780

Bryden, H. L., King, B. A., & McCarthy, G. D. (2011). South Atlantic overturning circulation at 24°S. *Journal of Marine Research*, *69*(1), 38–55. https://doi.org/10.1357/002224011798147633

Buckley, M. W., & Marshall, J. (2016). Observations, inferences, and mechanisms of the Atlantic Meridional Overturning Circulation: A review. *Reviews of Geophysics*, *54*(1), 5–63. https://doi.org/10.1002/2015RG000493

Caínzos, V., Hernández-Guerra, A., McCarthy, G. D., McDonagh, E. L., Cubas Armas, M., & Pérez-Hernández, M. D. (2022). Thirty Years of GOSHIP and WOCE Data: Atlantic Overturning of Mass, Heat, and Freshwater Transport. *Geophysical Research Letters*, *49*(4), 1–12. https://doi.org/10.1029/2021GL096527

de Carvalho Ferreira, M. L., & Kerr, R. (2017). Source water distribution and quantification of North Atlantic Deep Water and Antarctic Bottom Water in the Atlantic Ocean. *Progress in Oceanography*, *153*, 66–83. https://doi.org/10.1016/j.pocean.2017.04.003

Casanova-Masjoan, M., Pelegrí, J. L., Sangrà, P., Martínez, A., Grisolía-Santos, D., Pérez-Hernández, M. D., & Hernández-Guerra, A. (2017). Characteristics and evolution of an Agulhas ring. *Journal of Geophysical Research: Oceans*, *122*(9), 7049–7065. https://doi.org/10.1002/2017JC012969

Casanova-Masjoan, M., Pérez-Hernández, M. D., Vélez-Belchí, P., Cana, L., & Hernández-Guerra, A. (2020). Variability of the Canary Current Diagnosed by Inverse Box Models. *Journal of Geophysical Research: Oceans*, *125*(8). https://doi.org/10.1029/2020JC016199

Chidichimo, M. P., Piola, A. R., Meinen, C. S., Perez, R. C., Campos, E. J. D., Dong, S., et al. (2021). Brazil Current Volume Transport Variability During 2009–2015 From a Long-Term Moored Array at 34.5°S. *Journal of Geophysical Research: Oceans*, *126*(5). https://doi.org/10.1029/2020JC017146

Coachman, L. K., & Aagaard, K. (1988). Transports through Bering Strait: Annual and interannual variability. *Journal of Geophysical Research: Oceans*, *93*(C12), 15535. https://doi.org/10.1029/JC093iC12p15535

Coles, V. J., McCartney, M. S., Olson, D. B., & Smethie, W. M. (1996). Changes in Antarctic Bottom Water properties in the western South Atlantic in the late 1980s. *Journal of Geophysical Research C: Oceans*, *101*(C4), 8957–8970. https://doi.org/10.1029/95JC03721

Comas-Rodríguez, I., Hernández-Guerra, A., & McDonagh, E. L. (2010). Referencing geostrophic velocities using ADCP data Referencing geostrophic velocities using ADCP data. *Scientia Marina*, *74*(2), 331–338. https://doi.org/10.3989/scimar.2010.74n2331

Dong, S., Goni, G., & Bringas, F. (2015). Temporal variability of the South Atlantic Meridional Overturning Circulation between 20°S and 35°S. *Geophysical Research Letters*, *42*(18), 7655–7662. https://doi.org/10.1002/2015GL065603

Drévillon, M., Bahurel, P., Bazin, D., Benkiran, M., Beuvier, J., Crosnier, L., et al. (2018). Learning about Copernicus Marine Environment Monitoring Service "CMEMS": A Practical Introduction to the Use of the European Operational Oceanography Service. In *New Frontiers in Operational Oceanography*. GODAE OceanView. https://doi.org/10.17125/gov2018.ch25

ECCO Consortium, Fukumori, I., Wang, O., Fenty, I., Forget, G., Heimbach, P., & Ponte, R. M. (2020). ECCO central estimate (version 4 release 4). Retrieved from https://ecco.jpl.nasa.gov/drive/files/Version4/Release4/interp_monthly

ECCO Consortium, Fukumori, I., Wang, O., Fenty, I., Forget, G., Heimbach, P., & Ponte, R. M. (2021). Synopsis of the ECCO central production global ocean and sea-ice state estimate (version 4 release 4). *Zenodo*. https://doi.org/https://doi.org/10.5281/zenodo.4533349

Evans, G. R., McDonagh, E. L., King, B. A., Bryden, H. L., Bakker, D. C. E., Brown, P. J., et al. (2017). South Atlantic interbasin exchanges of mass, heat, salt and anthropogenic carbon. *Progress in Oceanography*,

151, 62–82. https://doi.org/10.1016/j.pocean.2016.11.005

Finucane, G., & Hautala, S. (2022). Transport of Antarctic Bottom Water entering the Brazil Basin in a Planetary Geostrophic Inverse Model. *Geophysical Research Letters*, 1–9. https://doi.org/10.1029/2022gl100121

Forget, G., Campin, J. M., Heimbach, P., Hill, C. N., Ponte, R. M., & Wunsch, C. (2015). ECCO version 4: An integrated framework for non-linear inverse modeling and global ocean state estimation. *Geoscientific Model Development*, *8*(10), 3071–3104. https://doi.org/10.5194/gmd-8-3071-2015

Fu, L.-L. (1981). The General Circulation and Meridional Heat Transport of the Subtropical South Atlantic Determined by Inverse Methods. *Journal of Physical Oceanography*, *11*(9), 1171–1193. https://doi.org/10.1175/1520-0485(1981)011<1171:TGCAMH>2.0.CO;2

Fukumori, I., Wang, O., Fenty, I., Forget, G., Heimbach, P., & Ponte, R. M. (2020). ECCO version 4 release 4.

Ganachaud, A. (2003). Large-scale mass transports, water mass formation, and diffusivities estimated from World Ocean Circulation Experiment (WOCE) hydrographic data. *Journal of Geophysical Research*, *108*(C7), 3213. https://doi.org/10.1029/2002JC001565

Ganachaud, A., & Wunsch, C. (2000). Improved estimates of global ocean circulation, heat transport and mixing from hydrographic data. *Nature*, *408*(6811), 453–457. https://doi.org/10.1038/35044048

Garzoli, S. L., & Gordon, A. L. (1996). Origins and variability of the Benguela Current. *Journal of Geophysical Research: Oceans*, *101*(C1), 897–906. Retrieved from http://dx.doi.org/10.1029/95JC03221

Garzoli, S. L., & Matano, R. (2011). The South Atlantic and the Atlantic Meridional Overturning Circulation. *Deep Sea Research Part II: Topical Studies in Oceanography*, *58*(17–18), 1837–1847. https://doi.org/10.1016/j.dsr2.2010.10.063

Garzoli, S. L., Baringer, M. O., Dong, S., Perez, R. C., & Yao, Q. (2013). South Atlantic meridional fluxes. *Deep Sea Research Part I: Oceanographic Research Papers*, *71*, 21–32. https://doi.org/10.1016/j.dsr.2012.09.003

Garzoli, S. L., Dong, S., Fine, R., Meinen, C. S., Perez, R. C., Schmid, C., et al. (2015). The fate of the Deep Western Boundary Current in the South Atlantic. *Deep Sea Research Part I: Oceanographic Research Papers*, *103*, 125–136. https://doi.org/10.1016/j.dsr.2015.05.008

Gordon, A. L. (1981). South Atlantic thermocline ventilation. *Deep Sea Research Part A. Oceanographic Research Papers*, *28*(11), 1239–1264. https://doi.org/10.1016/0198-0149(81)90033-9

Gordon, A. L. (1985). Indian-Atlantic transfer of thermocline water at the Agulhas retroflection. *Science*, *227*(4690), 1030–1033. https://doi.org/10.1126/science.227.4690.10

Gordon, A. L. (1986). Interocean exchange of thermocline water. *Journal of Geophysical Research*, *91*(C4), 5037. https://doi.org/10.1029/JC091iC04p05037

Gordon, A. L. (1989). Brazil-Malvinas Confluence–1984. *Deep Sea Research Part A. Oceanographic Research Papers*, *36*(3), 359–384. https://doi.org/10.1016/0198-0149(89)90042-3

Gordon, A. L., Weiss, R. F., Smethie, W. M., & Warner, M. J. (1992). Thermocline and intermediate water communication between the South Atlantic and Indian Oceans. *Journal of Geophysical Research*, *97*(C5), 7223. https://doi.org/10.1029/92JC00485

Guo, Y., Li, Y., & Wang, F. (2023). Destinations and pathways of the Indonesian Throughflow water in the Indian Ocean. *Journal of Climate*, 1–39. https://doi.org/10.1175/jcli-d-22-0631.1

Hernández-Guerra, A., & Talley, L. D. (2016). Meridional overturning transports at 30°S in the Indian and Pacific Oceans in 2002–2003 and 2009. *Progress in Oceanography*, *146*, 89–120. https://doi.org/10.1016/j.pocean.2016.06.005

Hernández-Guerra, A., Fraile-Nuez, E., López-Laatzen, F., Martínez, A., Parrilla, G., & Vélez-Belchí, P. (2005). Canary Current and North Equatorial Current from an inverse box model. *Journal of Geophysical Research: Oceans*, *110*(12), 1–16. https://doi.org/10.1029/2005JC003032

Hernández-Guerra, A., Pelegrí, J. L., Fraile-Nuez, E., Benítez-Barrios, V. M., Emelianov, M., Pérez-Hernández, M. D., & Vélez-Belchí, P. (2014). Meridional Overturning Transports at 7.5N and 24.5N in the Atlantic

Ocean during 1992-93 and 2010-11. *Progress in Oceanography*, *128*, 98–114. https://doi.org/10.1016/j.pocean.2014.08.016.

Hernández-Guerra, A., Talley, L. D., Pelegrí, J. L., Vélez-Belchí, P., Baringer, M. O., Macdonald, A. M., & McDonagh, E. L. (2019). The upper, deep, abyssal and overturning circulation in the Atlantic Ocean at 30°S in 2003 and 2011. *Progress in Oceanography*, *176*, 102136. https://doi.org/10.1016/j.pocean.2019.102136

Heywood, K. J., & King, B. A. (2002). Water masses and baroclinic transports in the South Atlantic and Southern oceans. *Journal of Marine Research*, *60*(5), 639–676.

Hogg, N., Biscaye, P., Gardner, W., & Sclunitz, W. J. (1982). On the transport and modification of Antarctic Bottom Water in the Vema Channel. *Journal of Marine Research*, *40*(23), 231–263.

Joyce, T. M., Hernández-Guerra, A., & Smethie, W. M. (2001). Zonal circulation in the NW Atlantic and Caribbean from a meridional World Ocean Circulation Experiment hydrographic section at 66 W. *Journal of Geophysical Research: Oceans*, *106*(C10), 22095–22113.

Kalnay, E., Kanamitsu, M., Kistler, R., Collins, W., Deaven, D., Gandin, L., et al. (1996). The NCEP/NCAR 40-Year Reanalysis Project. *Bulletin of the American Meteorological Society*, *77*(3), 437–471. https://doi.org/10.1175/1520-0477(1996)077<0437:TNYRP>2.0.CO;2

Karstensen, J. (2020, May 5). Physical oceanography (CTD) during Maria S. Merian cruise MSM60/1 [Dataset]. PANGAEA. https://doi.org/10.1594/PANGAEA.915898

Katsumata, K., & Fukasawa, M. (2011). Changes in meridional fluxes and water properties in the Southern Hemisphere subtropical oceans between 1992/1995 and 2003/2004. *Progress in Oceanography*, *89*(1–4), 61–91. https://doi.org/10.1016/j.pocean.2010.12.008

Kelly, K. A., Thompson, L., & Lyman, J. (2014). The Coherence and Impact of Meridional Heat Transport Anomalies in the Atlantic Ocean Inferred from Observations. *Journal of Climate*, *27*(4), 1469–1487. https://doi.org/10.1175/JCLI-D-12-00131.1

Kersalé, M., Perez, R. C., Speich, S., Meinen, C. S., Lamont, T., Le Hénaff, M., et al. (2019). Shallow and Deep Eastern Boundary Currents in the South Atlantic at 34.5°S: Mean Structure and Variability. *Journal of Geophysical Research: Oceans*, *124*, 1–26. https://doi.org/10.1029/2018JC014554.

Kersalé, M., Meinen, C. S., Perez, R. C., Piola, A. R., Speich, S., Campos, E. J. D., et al. (2021). Multi-Year Estimates of Daily Heat Transport by the Atlantic Meridional Overturning Circulation at 34.5°S. *Journal of Geophysical Research: Oceans*, *126*(5), 1–23. https://doi.org/10.1029/2020JC016947

Laxenaire, R., Speich, S., Blanke, B., Chaigneau, A., Pegliasco, C., & Stegner, A. (2018). Anticyclonic Eddies Connecting the Western Boundaries of Indian and Atlantic Oceans. *Journal of Geophysical Research: Oceans*, *123*(11), 7651–7677. https://doi.org/10.1029/2018JC014270

Lynch-Stieglitz, J. (2017). The Atlantic Meridional Overturning Circulation and Abrupt Climate Change. *Annual Review of Marine Science*, *9*(1), 83–104. https://doi.org/10.1146/annurev-marine-010816-060415

Majumder, S., & Schmid, C. (2018). A study of the variability in the Benguela Current volume transport. *Ocean Science*, *14*(2), 273–283. https://doi.org/10.5194/os-14-273-2018

Majumder, S., Schmid, C., & Halliwell, G. (2016). An observations and model-based analysis of meridional transports in the South Atlantic. *Journal of Geophysical Research: Oceans*, *121*(8), 5622–5638.

Manta, G., Speich, S., Karstensen, J., Hummels, R., Kersalé, M., Laxenaire, R., et al. (2021). The South Atlantic Meridional Overturning Circulation and Mesoscale Eddies in the First GO-SHIP Section at 34.5°S. *Journal of Geophysical Research: Oceans*, *126*(2), 1–25. https://doi.org/10.1029/2020JC016962

Mantyla, A. W., & Reid, J. L. (1983). Abyssal characteristics of the World Ocean waters. *Deep Sea Research Part A. Oceanographic Research Papers*, *30*(8), 805–833.

Matano, R. P., Palma, E. D., & Piola, A. R. (2010). The influence of the Brazil and Malvinas Currents on the Southwestern Atlantic Shelf circulation. *Ocean Science*, *6*(4), 983–995. https://doi.org/10.5194/os-6-983-2010

McDonagh, E. L., & King, B. A. (2005). Oceanic Fluxes in the South Atlantic. *Journal of Physical*

Oceanography, *35*(1), 109–122. https://doi.org/10.1175/JPO-2666.1

McDonagh, E. L., Bryden, H. L., King, B. A., & Sanders, R. J. (2008). The circulation of the Indian Ocean at 32°S. *Progress in Oceanography*, *79*(1), 20–36. https://doi.org/10.1016/j.pocean.2008.07.001

Meinen, C. S., & Garzoli, S. L. (2014). Attribution of deep western boundary current variability at 26.5ºN. *Deep Sea Research Part I: Oceanographic Research Papers*, *90*, 81–90. https://doi.org/http://dx.doi.org/10.1016/ j. dsr.2014.04.016.

Meinen, C. S., Speich, S., Perez, R. C., Dong, S., Piola, A. R., Garzoli, S. L., et al. (2013). Temporal variability of the meridional overturning circulation at 34.5°S: Results from two pilot boundary arrays in the South Atlantic. *Journal of Geophysical Research: Oceans*, *118*(12), 6461–6478. https://doi.org/10.1002/2013JC009228

Meinen, C. S., Garzoli, S. L., Perez, R. C., Campos, E., Piola, A. R., Chidichimo, M. P., et al. (2017). Characteristics and causes of Deep Western Boundary Current transport variability at 34.5° S during 2009-2014. *Ocean Science*, *13*(1), 175–194. https://doi.org/10.5194/os-13-175-2017

Meinen, C. S., Speich, S., Piola, A. R., Ansorge, I., Campos, E., Kersalé, M., et al. (2018). Meridional Overturning Circulation Transport Variability at 34.5°S During 2009–2017: Baroclinic and Barotropic Flows and the Dueling Influence of the Boundaries. *Geophysical Research Letters*, *45*(9), 4180–4188. https://doi.org/10.1029/2018GL077408

Mercier, H., Arhan, M., & Lutjeharms, J. R. E. (2003). Upper-layer circulation in the eastern Equatorial and South Atlantic Ocean in January-March 1995. *Deep-Sea Research Part I: Oceanographic Research Papers*, *50*(7), 863–887. https://doi.org/10.1016/S0967-0637(03)00071-2

Moffa-Sánchez, P., & Hall, I. R. (2017). North Atlantic variability and its links to European climate over the last 3000 years. *Nature Communications*, *8*(1), 1726. https://doi.org/10.1038/s41467-017-01884-8

Müller, T. J., Ikeda, Y., Zangenberg, N., & Nonato, L. V. (1998). Direct measurements of western boundary currents off Brazil between 20°S and 28°S. *Journal of Geophysical Research: Oceans*, *103*(C3), 5429–5437. https://doi.org/10.1029/97JC03529

Palma, E. D., & Matano, R. P. (2017). South Atlantic circulation and variability from a data assimilating model. In *Marine pollution and climate change* (pp. 39–65). CRC Press.

Palter, J. B. (2015). The role of the Gulf Stream in European climate. *Annual Review of Marine Science*, *7*(1), 113–137. https://doi.org/10.1146/annurev-marine-010814-015656

Perez, R. C., Garzoli, S. L., Meinen, C. S., & Matano, R. P. (2011). Geostrophic velocity measurement techniques for the meridional overturning: Circulation and meridional heat transport in the South Atlantic. *Journal of Atmospheric and Oceanic Technology*, *28*(11), 1504–1521. https://doi.org/10.1175/JTECH-D-11-00058.1

Peterson, R. G., & Stramma, L. (1991). Upper-level circulation in the South Atlantic Ocean. *Progress in Oceanography*, *26*(1), 1–73. https://doi.org/10.1016/0079-6611(91)90006-8

Peterson, R. G., & Whitworth, T. (1989). The subantarctic and polar fronts in relation to deep water masses through the southwestern Atlantic. *Journal of Geophysical Research*, *94*(C8), 10817. https://doi.org/10.1029/JC094iC08p10817

Poole, R., & Tomczak, M. (1999). Optimum multiparameter analysis of the water mass structure in the Atlantic Ocean thermocline. *Deep Sea Research Part I: Oceanographic Research Papers*, *46*(11), 1895–1921. https://doi.org/10.1016/S0967-0637(99)00025-4

Reid, J. L. (1989). On the total geostrophic circulation of the South Atlantic Ocean: Flow patterns, tracers, and transports. *Progress in Oceanography*, *23*(3), 149–244. https://doi.org/10.1016/0079-6611(89)90001-3

Reid, Joseph L., Nowlin, W. D., & Patzert, W. C. (1977). On the Characteristics and Circulation of the Southwestern Atlantic Ocean. *Journal of Physical Oceanography*, *7*(1), 62–91. https://doi.org/10.1175/1520-0485(1977)007<0062:OTCACO>2.0.CO;2

Richardson, P. L., & Garzoli, S. L. (2003). Characteristics of intermediate water flow in the Benguela current as measured with RAFOS floats. *Deep-Sea Research Part II: Topical Studies in Oceanography*, *50*(1),

87–118. https://doi.org/10.1016/S0967-0645(02)00380-6

Rodrigues, R. R., Rothstein, L. M., & Wimbush, M. (2007). Seasonal Variability of the South Equatorial Current Bifurcation in the Atlantic Ocean: A Numerical Study. *Journal of Physical Oceanography*, *37*(1), 16–30. https://doi.org/10.1175/JPO2983.1

Schmid, C., & Majumder, S. (2018). Transport variability of the Brazil Current from observations and a data assimilation model. *Ocean Science*, *14*(3), 417–436.

van Sebille, E., England, M. H., & Froyland, G. (2012). Origin, dynamics, and evolution of ocean garbage patches from observed surface drifters. *Environmental Research Letters*, *7*(4), 044040. https://doi.org/https://doi.org/10.1088/1748-9326/7/4/044040

Shannon, L. V., & Hunter, D. (1988). Notes on Antarctic intermediate water around southern Africa. *South African Journal of Marine Science*, *6*(1), 107–117. https://doi.org/10.2989/025776188784480735

Sloyan, B. M., & Rintoul, S. R. (2001). The Southern Ocean Limb of the Global Deep Overturning Circulation*. *Journal of Physical Oceanography*, *31*(1), 143–173. https://doi.org/10.1175/1520-0485(2001)031<0143:TSOLOT>2.0.CO;2

Speer, K. G., Siedler, G., & Talley, L. (1995). The Namib Col Current. *Deep Sea Research Part I: Oceanographic Research Papers*, *42*(11–12), 1933–1950. https://doi.org/10.1016/0967-0637(95)00088-7

Speich, S., Blanke, B., & Madec, G. (2001). Warm and cold water routes of an O.G.C.M. thermohaline conveyor belt. *Geophysical Research Letters*, *28*(2), 311–314. https://doi.org/10.1029/2000GL011748

Sprintall, J., & Tomczak, M. (1993). On the formation of Central Water and thermocline ventilation in the southern hemisphere. *Deep-Sea Research Part I: Oceanographic Research Papers*, *40*(4), 827–848.

Stramma, L. (1989). The Brazil current transport south of 23°S. *Deep Sea Research Part A. Oceanographic Research Papers*, *36*(4), 639–646. https://doi.org/10.1016/0198-0149(89)90012-5

Stramma, L. (1991). Geostrophic transport of the South Equatorial Current in the Atlantic. *Journal of Marine Research*, *49*(2), 281–294. https://doi.org/10.1357/002224091784995864

Stramma, L., & England, M. (1999). On the water masses and mean circulation of the South Atlantic Ocean. *Journal of Geophysical Research: Oceans*, *104*(C9), 20863–20883. https://doi.org/10.1029/1999JC900139

Suga, T., & Talley, L. D. (1995). Antarctic Intermediate Water circulation in the tropical and subtropical South Atlantic. *Journal of Geophysical Research*, *100*(C7), 13441. https://doi.org/10.1029/95JC00858

Talley, L. D. (1996). Antarctic Intermediate Water in the South Atlantic. In *The South Atlantic* (pp. 219–238). Berlin, Heidelberg: Springer Berlin Heidelberg. https://doi.org/10.1007/978-3-642-80353-6_11

Talley, L. D. (2003). Shallow, Intermediate, and Deep Overturning Components of the Global Heat Budget. *Journal of Physical Oceanography*, *33*(3), 530–560. https://doi.org/10.1175/1520-0485(2003)033<0530:SIADOC>2.0.CO;2

Talley, L. D. (2008). Freshwater transport estimates and the global overturning circulation: Shallow, deep and throughflow components. *Progress in Oceanography*, *78*(4), 257–303. https://doi.org/10.1016/j.pocean.2008.05.001

Talley, L. D. (2013). Closure of the Global Overturning Circulation Through the Indian, Pacific, and Southern Oceans: Schematics and Transports. *Oceanography*, *26*(1), 80–97. https://doi.org/10.5670/oceanog.2013.07

Talley, L. D., & McCartney, M. S. (1982). Distribution and Circulation of Labrador Sea Water. *Journal of Physical Oceanography*, *12*(11), 1189–1205. https://doi.org/10.1175/1520-0485(1982)012<1189:DACOLS>2.0.CO;2

Talley, L. D., Pickard, G. L., Emery, W. J., & Swift, J. H. (2011). *Descriptive Physical Oceanography: An Introduction* (Sixth). B: Elsevier Ltd.

Talley, L. D., Feely, R. A., Sloyan, B. M., Wanninkhof, R., Baringer, M. O., Bullister, J. L., et al. (2016). Changes in Ocean Heat, Carbon Content, and Ventilation: A Review of the First Decade of GO-SHIP

Global Repeat Hydrography. *Annual Review of Marine Science*, *8*(1), 185–215. https://doi.org/10.1146/annurev-marine-052915-100829

Toole, J. M., Curry, R. G., Joyce, T. M., McCartney, M., & Peña-Molino, B. (2011). Transport of the North Atlantic Deep Western Boundary Current about 39°N, 70°W: 2004–2008. *Deep Sea Research Part II: Topical Studies in Oceanography*, *58*(17–18), 1768–1780. https://doi.org/10.1016/j.dsr2.2010.10.058

Vanicek, M., & Siedler, G. (2002). Zonal fluxes in the deep water layers of the western South Atlantic Ocean. *Journal of Physical Oceanography*, *32*(8), 2205–2235. https://doi.org/10.1175/1520-0485(2002)032<2205:ZFITDW>2.0.CO;2

Wang, O., Fukumori, I., & Fenty, I. (2020). ECCO version 4 release 4 user guide.

Warren, B. A., & Speer, K. G. (1991). Deep circulation in the eastern South Atlantic Ocean. *Deep Sea Research Part A. Oceanographic Research Papers*, *38*, S281–S322. https://doi.org/10.1016/S0198-0149(12)80014-8

Wunsch, C. (1978). The North Atlantic general circulation west of 50°W determined by inverse methods. *Reviews of Geophysics*, *16*(4), 583–620. https://doi.org/10.1029/RG016i004p00583

Wunsch, C. (1996). *The Ocean Circulation Inverse Problem*. Cambridge University Press. https://doi.org/10.1017/CBO9780511629570

Zemba, J. C. (1991). *The Structure and Transport of the Brazil Current between 27^o and 36^o South.* Massachusetts Institute of Technology and Woods Hole Oceanographic Institution.

Zenk, W., Siedler, G., Lenz, B., & Hogg, N. G. (1999). Antarctic Bottom Water Flow through the Hunter Channel. *Journal of Physical Oceanography*, *29*(11), 2785–2801. https://doi.org/10.1175/1520-0485(1999)029<2785:ABWFTT>2.0.CO;2